RICE UNIVERSITY

Recovery of neuronal channel densities from calcium fluorescence

by

Jay Raol

A Thesis Submitted
in Partial Fulfillment of the
Requirements for the Degree

Doctorate of Philosophy

Approved, Thesis Committee:

Steven J. Cox, Chairman
Professor of Computational and Applied Mathematics

Robin Forman
Professor of Mathematics

Matthias Heinkenschloss
Professor of Computational and Applied Mathematics

Houston, Texas

May, 2010

Abstract

Recovery of neuronal channel densities from calcium fluorescence

by

Jay Raol

Neurons have the ability to dynamically adjust their own membrane channel densities to modulate the strength of communication with other neurons. This process is integral to such neuronal functions as spatial recognition and memory but has been difficult to measure experimentally. Historically, neuroscientists have used changes in voltage to infer changes in neuronal channel densities. However, voltage is difficult to measure away from the soma. Many important functions in the neuron, like synaptic integration, take place in the dendritic tree where traditional voltage measurements can not be taken. To interrogate the neuron in the dendrites, experimentalists have come to rely on calcium fluorescence based microscopy to infer qualitative information about voltage changes in the dendrites. In these experiments, intracellular calcium changes due to voltage depolarizations are recorded at spatially distributed sites on the dendrites through the binding of calcium to a fluorescent buffer. The recovery of channel densities can be posed as a parameter identification problem in a coupled nonlinear partial differential equation that relates the responses of calcium, the fluorescent buffer and voltage to neuronal stimulation. We convert temporally and spatially distributed fluorescence data into quantitative measurements of voltage sensitive channel densities by inverting slow time–scaled calcium data into fast

time–scaled voltage data. Our approach is to solve four interrelated inverse problems corresponding to three different proposed experiments to go from calcium fluorescence to channel densities. In the first experiment, we use subthreshold calcium dynamics to infer the reaction kinetics between calcium and fluorescent buffer. From these kinetics, we can use suprathreshold voltage stimulation to infer calcium channel densities and recover distributed voltage data. Finally, we use the voltage data to infer potassium channel densities in the dendrites. Our algorithm has been shown to recover channel densities for several different calcium channel models and the delayed rectifying potassium channel from simulated noisy fluorescence data in morphologically realistic neurons.

Contents

List of Figures

List of Tables

Chapter 1

Introduction

1.1 Thesis Overview

Understanding learning and memory mechanisms in the brain requires the ability to measure individual neuronal properties for many different neurons in the brain. Due to technical limitations in current experimental setups, it is not possible to quickly gather this information. Currently, a typical experiment uses calcium based fluorescence to qualitatively infer neuronal properties. We developed an algorithm to quickly and automatically convert calcium fluorescence data into quantitative measurements of neuronal channel densities.

In the following introduction, we will motivate the relationship between the section of the neuron known as the dendritic tree and synaptic integration. We shall then discuss how calcium imaging has become the primary tool in experimentally understanding synaptic integration. In parallel, we shall also review the central role mathematical modeling has had in understanding properties of the dendrites. Finally, we shall elaborate on the work we have done to convert calcium fluorescence data to channel densities which relies on unifying current experiments with a mathematical description of the dendrites.

1.2 Synaptic integration and the properties of dendrites

The neuron is the fundamental building block for learning and memory. A neuron is a specialized cell in the brain that receives inputs from many other neurons and fires an action potential in response. Neurons connect to each other at specialized junctions called synapses. These protrusions on the dendrites modulate the strength of incoming signals from other neurons. Synaptic integration is the process by which action potentials are sculpted by synaptic responses as they travel down dendrites toward the soma. Initially, this process was thought to be purely algebraic in nature [47], [4]. However, recent experimental evidence [8], [23], [36], [64] has shown that interactions between synapses are mediated through active and passive dendritic properties which together participate in synaptic integration.

The passive properties of the dendrites include the membrane capcitance, axial resistivity and the dendritic geometry. Figure 1.1(b) shows an example of the extensive geometry found in neurons of the brain. The membrane capcitance and axial resistivity has been experimentally shown to remain relatively constant in different neurons of the brain. However, the geometry of the dendritic tree varies between different neurons.

The active properties of the dendrites refer to the different membrane channels that dynamically alter membrane conductance in a voltage dependent manner. The sodium channel is the primary means of driving large depolarizations in the dendrites through an inward current. The potassium channel hyperpolarizes the cell through a strong outward current. Together, potassium and sodium channels are the main mechanisms of synaptic integration in the cell. Sodium channels are the primary means of supporting back propagating action potentials and amplifying distal synaptic input. Potassium channels regulate local synaptic input and spike initiation. Calcium channels depolarize the cell with a small inward current. Their primary task seems

to center around converting voltage changes into calcium concentration changes in the cell. As we will discuss later, calcium changes can lead to short-term and long-term changes in dendritic excitability. Calcium can also modulate the strength of synaptic inputs. Finally, there are other voltage sensitive channels like chloride and hyperpolarizing cation channels. All the ionic channels help to dampen, amplify and shape the impulses that pass through the dendrites. Unlike the passive properties of a neuron, the active properties differ widely between different neurons. Therefore, the process of synaptic integration is highly dependent on the different channel densities in the dendritic tree. Unfortunately, these densities can not be easily measured.

1.3 Inferring active properties with calcium imaging

Until recently, the only direct way of measuring any relevant information about a neuron was through either patch pipette or microelectrode impalement. At first, these techniques could only be applied at the neuron's soma. Extracellular field potential recordings first hinted at the possibility of active dendrites. With the advent of new infrared imaging techniques, the experimentalist could directly patch or impale large dendrites. However, these techniques are still confined to thicker sections of the tree and can only collect local information about the dendrites [35], [66].

Additionally, there have been a great number of biochemical assays that can probe dendrites. Antibodies can be used for immunohistochemical quantification of channel types and densities. Genetic modification can be used to change dendritic properties though viral transfection. Finally, advanced microscopy techniques can visualize the dendritic surface to identify and quantify channels.

Although these techniques are currently the only quantitative assay for dendritic channel densities, they can be expensive and time consuming. Therefore, experimentalists have turned to ionic and voltage sensitive dyes. When combined with

high-speed fluorescence imaging, the experimentalist can quickly infer the properties of dendrites. The calcium based dyes have become the most popular choice in these experiments for several reasons.

Calcium is arguably the most important ion in the neuron. At rest, intracellular calcium is kept at extremely small concentrations compared to the extracellular concentration. In addition, there are internal organelles, mainly mitochondria and the endoplasmic reticulum (ER), that serve as large internal stores. Calcium interacts with the neuron through calcium binding proteins which can trigger a chain reaction of different behavior. This can include regulation of local and global transcription of genes, release of calcium from internal stores and other functions. For example, Perkel et al. [56] showed in figure 1.1(a) that calcium entry occurs in the synapse via NMDA receptors during long-term potentiation.

This dual nature of calcium as an important reporter ion and primary second messenger has complicated the interpretation of fluorescence data arising from calcium imaging based experiments. One problem arises in inferring calcium concentrations from fluorescence data. Fluorescence data actually measures changes in the amount of calcium bound dye concentrations. However, depending on the type of dye, calcium concentrations may not parallel calcium bound dye concentrations.

Beyond the problem of interpreting fluorescence data, injecting a neuron with a large concentration of calcium dye skews the internal mechanics of calcium regulation. Calcium is usually controlled very tightly, both temporally and spatially, through membrane bound pumps and calcium binding proteins. The addition of a calcium dye greatly increases the amount of mobile calcium buffers. The calcium dye will bind calcium and diffuse away from the source before releasing some of it. This has the net effect of an elevated calcium concentration in a broader area and over a greater time period than what would naturally occur. The diffusible nature of the buffer makes inferring the actual calcium concentration more difficult.

Despite these drawbacks, calcium dyes are extremely useful. They have the highest

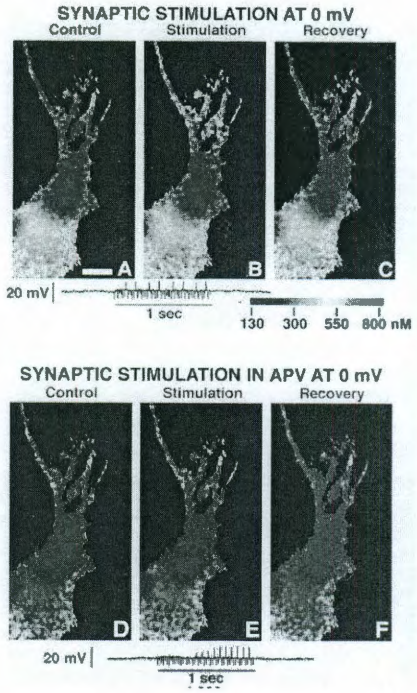

(a)

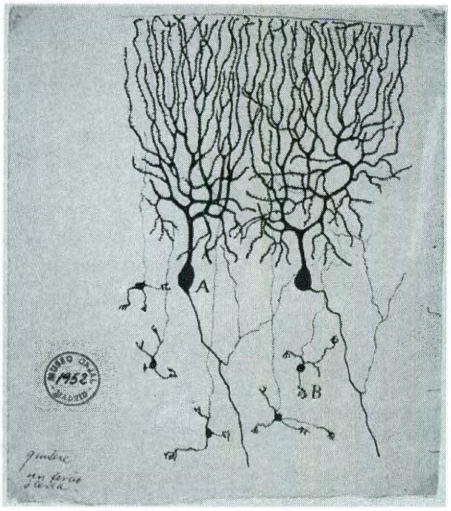

(b)

Figure 1.1: In figure (a) fluorescence images from calcium bound dye taken at three sequential time points during a learning protocol are shown [56]. The top panel shows increased calcium concentrations during learning. In the presence of a learning inhibitor, the bottom panel, shows, as a control, no calcium flux into the synapses. This experiment proved calcium's important role in learning and memory. In figure 1.1(b), a stained neuron shows the complexity of dendritic geometry.

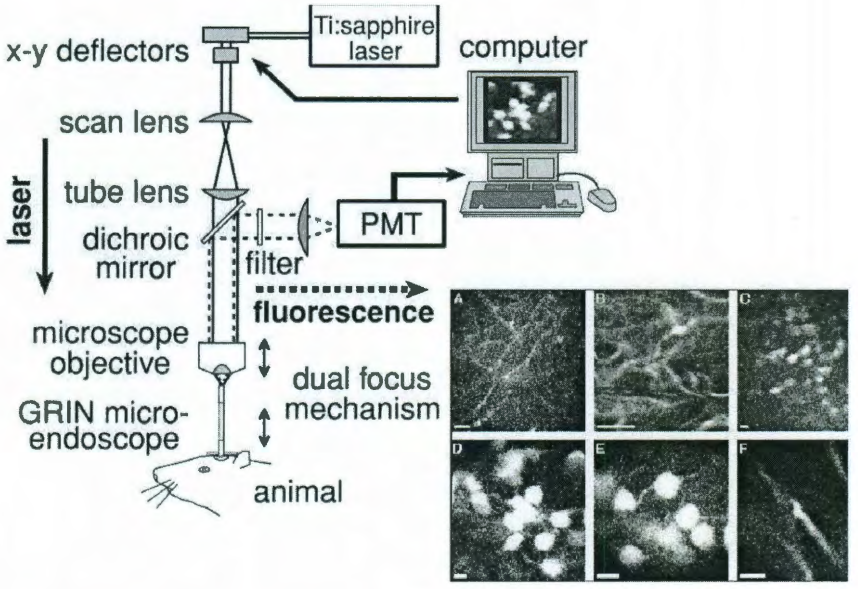

Figure 1.2: The following pictorially illustrates the increasing role of calcium based fluorescence in *in vivo* studies of neural networks. A small two-photon microscope is mounted on a live rat. Fluorescence data of the visual cortex during a spatial navigation experiment is measured and recorded. From this data, firing rates for the observed neurons are inferred based on the relationship between calcium and the membrane potential firing rate.

signal-to-noise ratio of the ion based dyes. Because calcium contributes relatively little to the inward current, interactions between the dye and calcium do not alter the action potential. The presence of voltage sensitive calcium channels allows calcium dye fluorescence to be used as a surrogate for the firing rate of a neuron. Finally, fluorescence based imaging can be combined with two-photon microscopy to achieve spatially and temporally distributed data from *in vivo* preparations. In figure 1.2, microendoscope based two-photon microscopy combined with calcium imaging is used to infer *in vivo* firing rates of neurons.

1.4 Recovery of the active dendritic properties

We solve a series of interrelated inverse problems that take advantage of the large amounts of fluorescence data from calcium based imaging to uncover active dendritic properties of the neuron. Specifically, we can quantify the channel densities in the dendrites that lead to spatio-voltage specific conductance changes in the process of synaptic integration. We begin by modeling the response of calcium, buffer and voltage through coupled nonlinear parabolic equations.

The recovery of channel densities can then be posed as a parameter identification problem using fluorescence data. We break up this inverse problem into four sub problems which reflect natural segmentations in the corresponding experimental approach. The first sub problem deals with accurately recovering calcium currents from fluorescence data. This requires knowledge of parameters in the chemical reaction between calcium and its buffer while accounting for the diffusible nature of both calcium and the buffer. The second sub problem deals with the recovery of calcium currents from fluorescence data. The third problem is to invert Ohm's Law and recover voltage and calcium channel densities from calcium current. The final sub problem uses the voltage data extracted from calcium currents to determine the potassium channel densities.

In 2.1, we explain the nonlinear parabolic equations that describe the voltage response in the neuron to stimulation. In 2.3, we build a model of calcium that incorporates only the most salient interactions between calcium, the fluorescent dye and voltage. In 3.1, we will first review the different approaches used to infer different neuronal properties of interest. Then we will bring the calcium and voltage models together and pose the problem we wish to solve within the framework of available data and *a priori* known quantities. In 3.5, we discuss finding the passive calcium system parameters. In 3.6, we step through a simple procedure to find the calcium current from calcium bound buffered data. In 3.7, we discuss specific channel models that allow us to invert Ohm's Law and recover the calcium conductance and voltage from the current. Finally, in 3.8, we use the recovered voltage in 3.7 to recover potassium channel densities.

Chapter 2

The forward problem

In the following chapter, we will review the models that describe the dynamics of calcium and voltage in the neuron. Briefly, the voltage equations can be derived by applying Kirchhoff's Law to all of the current sources in a neuron. This includes voltage–sensitive calcium channels. These channels act as sources of calcium that can then interact through chemical reactions with a diffusible fluorescent buffer. Since we are also interested in the spatial dynamics of this system, special consideration must be made to describe the equation of the calcium–voltage system on the geometry of the dendritic arbor. We end this chapter by describing the different types of calcium channels that can couple the calcium and voltage equations. The numerical solutions to these systems will be the simulated data that is inverted to find channel densities.

2.1 Hodgkin-Huxley model of wave propagation

In the 1930's and 1940's, Kenneth Cole and collaborators carried out a series of experiments using electrodes placed down the length of a giant axon of the squid. They uncovered the relationship between the membrane potential and the firing of an action potential. Cole's use of the voltage clamp allowed investigators for the first time to measure and separate the different ionic currents that arise from the large

conductance change during action potential firing [9]. A decade later, Alan Hodgkin and Andrew Huxley were able to write down the mathematical equations that govern the large conductance change associated with the firing of an action potential [33]. The contribution by Hodgkin and Huxley was to parse the large conductance change into three different associated ionic currents, Na, K and Cl. Together these currents act in a voltage dependent manner to depolarize the cell and bring it back to rest. Hodgkin and Huxley were able to write down the voltage dependence underpinning the ionic current through the use of gating variables. Specifically, the gating kinetics which can viewed as the open channel probability govern the associated current generated by the voltage depolarization. With the relationship between the voltage and the specific ionic currents known, we can write the following nonlinear parabolic equation for the transmembrane potential

$$\begin{aligned} C_m\partial_t v = G_i\partial_{xx}v - g_L(v-E_L) - n^4 g_K(v-E_K) - g_{Na}m^3h(v-E_{Na}) \\ - I_{Ca}(x,t) - I(t)\delta(x-x_0) \\ \partial_t n = \frac{n_\infty(v)-n}{\tau_n}, \quad \partial_t m = \frac{m_\infty(v)-m}{\tau_m}, \quad \partial_t h = \frac{h_\infty(v)-h}{\tau_h} \end{aligned} \tag{2.1}$$

where v satisfies the no flux boundary conditions

$$\partial_x v(0,t) = \partial_x v(l,t) = 0 \tag{2.2}$$

for a length l (cm) fiber with radius a (cm). E_L, E_K and E_{Na} (mV) are the transmembrane driving potentials determined by Nernst's equation. g_K, g_L and g_{Na} are the conductance densities (mS/cm^2) associated with their respective channels. C_m (mF/cm^2) is the membrane capacitance density. G_i (mS) is the axial conductivity computed from the axial resistance by $G_i = a/(2R_i)$. $I_{Ca}(x,t)$ (μA/cm^2) is the current density associated with voltage–sensitive calcium channels. In the experimental setting, we denote by $I(t)$ (μA/cm^2) the injected current density on the neuronal fiber at the point x_0. Finally, when we consider the fiber in the rest state, then

$v(x,0) \equiv v_0(x)$ satisfies the following

$$\begin{aligned} G_i v_0''(x) = g_L(x)(v_0(x) - E_L) + g_K(x) n_\infty(v_0(x))^4 (v_0(x) - E_K) \\ + g_{Na}(x) m_\infty(v_0(x))^3 h(v_0(x))(v_0(x) - E_{Na}) + I_{Ca}(x,0) \end{aligned} \tag{2.3}$$

The functional forms of the kinetic equations in (2.1) are given in table A.4. We now shall rewrite (2.1) in a more compact form for ease of exposition adopted from Kellems et al. [39],

$$\begin{aligned} C_m \partial_t v &= G_i \partial_{xx} v - \sum_{c=1}^{C} g_c(x)(v - E_c) \prod_{f=1}^{F_c} w_{cf}^{q_{cf}} - I(t)\delta(x - x_0) - I_{Ca}(x,t) \\ \partial_t w_{cf} &= \frac{w_{cf,\infty}(v) - w_{cf}}{\tau_{cf}(v)}, \end{aligned} \tag{2.4}$$

with the associated boundary conditions, $v_x(0,t) = v_x(l,t) = 0$ whose initial conditions $v(x,0) \equiv v_0(x)$ satisfy the following equation

$$G_i v_0'' - \sum_{c=1}^{C} g_c(x)(v_0 - E_c) \prod_{f=1}^{F_c} w_{cf,\infty}^{q_{cf}}(v_0) - I_{Ca}(x,t) = 0\,. \tag{2.5}$$

We have indexed the sets $\{g_L, g_K, g_{Na}\}$ and $\{E_L, E_K, E_{Na},\}$ by $c = 1, ..., C\,(= 3)$ and similarly for each set of gating variables (and their powers) associated with a given conductance, c. For example, the sodium gating variables are described by the set $\{m, h\}$ which is indexed by $f = 1..F_3\,(= 2)$ and powers $\{q_{31}, q_{32}\} = \{3, 1\}$. We shall utilize (2.4) when the need for compact notation dictates it. However, in general, we always refer to (2.1) as the system of interest.

2.2 Branched neuron

We follow Cox and Raol [17] in describing the extension of (2.4) to the case of branched dendritic tree. For simplicity, we assume that each branch point has exactly three branches, one parent and two children, and the tree has a single root. We consider B branches with S branch points. The kth branch point has a parent, p_k, and two

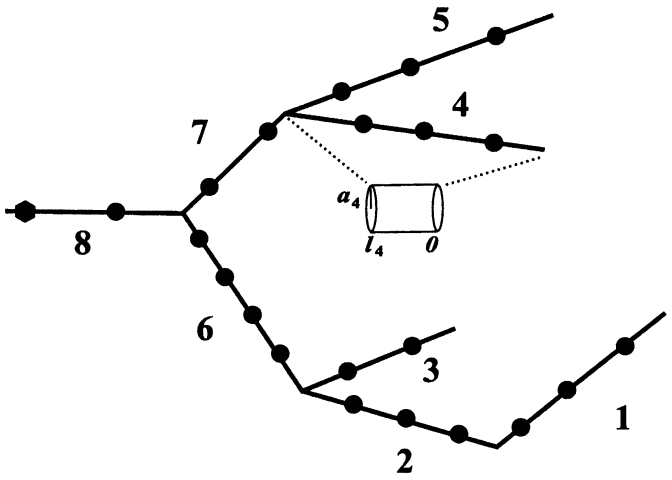

Figure 2.1: In this simplified tree structure, the branches are labeled according to the Hines scheme.

children, c_k^1 and c_k^2. For branches without children, leaves, we denote E as the set of leaf indices. The radius and length of a branch b is a_b and l_b, respectively in cm. Additionally, we follow the Hines [31] ordering scheme, whereby branches farthest from the root are numbered first. This is graphically shown in figure 2.2. Borrowing the same notational use of parameters from (2.4), the voltage at the bth branch, $v_b(x,t)$, satisfies

$$\begin{aligned} C_m \partial_t v_b &= G_{b_i} \partial_{xx} v_b - \sum_{c=1}^{C} g_{b_c}(x)(v - E_c) \prod_{f=1}^{F_c} w_{b_{cf}}^{q_{cf}} - I(t)\delta(x - x_0)\delta_{b,b_0} - I_{Ca,b}(x,t) \\ \partial_t w_{b_{cf}} &= \frac{w_{cf,\infty}(v_b) - wb_{cf}}{\tau_{cf}(v_b)}, \quad b = 1, ..., B \quad 0 < x < l_b, \quad t > 0 \end{aligned} \tag{2.6}$$

where δ_{b,b_0} is the Kronecker delta function that ensures current injection at the point x_0 on branch b_0 and $I_{Ca,b}$ is the calcium current density at the bth branch. At the branch points we enforce continuity of the voltage with

$$v_{p_k}(l_{p_k}, t) = v_{c_k^1}(0,t) = v_{c_k^2}(0,t) \tag{2.7}$$

and conservation of current with

$$a_{p_k}^2 \partial_x v_{p_k}(l_{p_k}, t) = a_{c_k^1}^2 \partial_x v_{c_k^1}(0, t) + a_{c_k^2}^2 \partial_x v_{c_k^2}(0, t)\,. \tag{2.8}$$

Finally, at the root and leafs, we have sealed ends yielding

$$\begin{aligned} \partial_x v_B(0, t) &= 0 \\ \partial_x v_b(l_b, t) &= 0, \quad b \in E \end{aligned} \tag{2.9}$$

and the initial conditions satisfy

$$G_i v_{0,b}'' - \sum_{c=1}^{C} g_c(x)(v_{0,b} - E_c) \prod_{f=1}^{F_c} w_{bcf,\infty}^{q_{cf}}(v_{0,b}) = 0\,. \tag{2.10}$$

With these equations, we can now model the voltage response in a branched dendritic tree to direct current injection.

2.3 Calcium in the presence of buffer

In a neuron, calcium plays a profound role in initiating internal changes in cellular physiology. The intracellular concentration of calcium is kept around 100 nM. This can be almost 10000 times smaller than the extracellular concentration. As a result, there is a strong gradient being maintained by the cell. This is accomplished by pumps and exchanges along the plasma membrane and the endoplasmic reticulum membrane. There are many different types of channels giving rise to a plethora of observed calcium dynamics. In addition to membrane bound channels, large proteins, both mobile and immobile, found in the cytoplasmic milieu bind calcium with varying speeds and affinity. The net result is a very complex dynamic when calcium enters the cell. To capture this dynamic in a simple way, we take into account only a few of the many process to model calcium dynamics. First, we consider the following reaction to account for mobile calcium buffers in the cell

$$\mathrm{c} + \mathrm{B} \underset{k_p}{\overset{k_m}{\rightleftharpoons}} \mathrm{b} \tag{2.11}$$

where c is calcium, B is unbound buffer and b is calcium bound buffer. The forward and backward reaction rates given by k_p and k_m are in units $(\mu\mathrm{M\ ms})^{-1}$ and ms^{-1}, respectively. We consider the standard model for calcium in the presence of mobile buffer given in more detail in [65] and [40] and derived in A.4. We consider again a fiber of length l (cm) with radius a (cm). The concentrations of calcium, c, and calcium bound buffer, b, are governed by

$$\begin{aligned} \partial_t b &= D_b \partial_{xx} b + k_p c(\mathcal{B} - b) - k_m b \\ \partial_t c &= D_c \partial_{xx} c - k_p c(\mathcal{B} - b) + k_m b - r(c - c_0) - 2\pi \frac{I_{Ca}}{aF} \end{aligned} \tag{2.12}$$

where the binding kinetics are from (2.11), r (ms^{-1}) is the extrusion pump rate and c_0 (μM) is steady-state intracellular calcium concentration. The respective diffusivites of calcium and bound buffer are given by D_c $(\mathrm{cm}^2/\mathrm{ms})$ and D_b $(\mathrm{cm}^2/\mathrm{ms})$. $\mathcal{B}$ $(\mu\mathrm{M})$ is the total buffer concentration and F $(\mathrm{C}/\mu\mathrm{mol})$ is Faraday's constant. Since we are

building a coupled system between voltage and calcium, we assume the only source of calcium is through voltage gated calcium channels. Hence, the source term in (2.12) is the outward calcium current converted to a concentration via Faraday's constant. (2.12) satisfies the no flux boundary conditions

$$\partial_x b(0,t) = \partial_x b(l,t) = \partial_x c(0,t) = \partial_x c(l,t) = 0 \tag{2.13}$$

and the following rest condition

$$c(x,0) = c_0, \quad b(x,0) = \frac{k_p c(x,0)\mathcal{B}}{k_p c(x,0) + k_m} = \frac{c_0 \mathcal{B}}{c_0 + K_d}. \tag{2.14}$$

Here, K_d is referred to as the disassociation constant which is an experimentally measured constant.

2.4 Calcium–buffer system in branched dendrites

Similar to the branched case previously discussed for the voltage equations, we can easily extend these equations using the same conditions. We consider B branches with S branch points. The kth branch point has a parent, p_k, and two children, c_k^1 and c_k^2. For branches without children, leaves, we denote E as the set of leaf indices. The radius and length of a branch j is a_j and l_j respectively in cm. Additionally, we follow the Hines [31] ordering scheme whereby branches farthest from the root are numbered first. Then c and b at the jth branch, $c_j(x,t)$ and $b_j(x,t)$, satisfies

$$\begin{aligned}
\partial_t b_j &= D_b \partial_{xx} b_j + k_p c_j(\mathcal{B} - b_j) - k_m b_j \\
\partial_t c_j &= D_c \partial_{xx} c_j - k_p c_j(\mathcal{B} - b_j) + k_m b_j - r(c_j - c_0) - 2\pi \frac{I_{Ca_j}}{a_j F} \\
j &= 1, \cdots, B \quad 0 < x < l_j \quad t > 0 .
\end{aligned} \tag{2.15}$$

At the branch points, continuity of the solution is enforced with

$$y_{p_k}(l_{p_k}, t) = y_{c_k^1}(0,t) = y_{c_k^2}(0,t) \quad y = [b,\, c] \tag{2.16}$$

and conservation of flux

$$a_{p_k}\partial_x y_{p_k}(l_{p_k},t) = a_{c_k^1}\partial_x y_{c_k^1}(0,t) + a_{c_k^2}\partial_x y_{c_k^2}(0,t) \quad y=[b,\,c]\,. \tag{2.17}$$

At the roots and leafs, we enforce the no flux condition

$$\partial_x y_B(0,t) = \partial_x y_j(l_j,t) = 0, \quad j\in E \quad y=[b,\,c] \tag{2.18}$$

and the initial conditions satisfy

$$c_j(x,0) = c_0, \quad b_j(x,0) = \frac{c_0\mathcal{B}}{c_0+K_d} \quad \forall j\,. \tag{2.19}$$

2.5 Voltage-gated calcium channels

In (2.12), the source term arises from the calcium current that occurs during membrane depolarization. Although this ignores the other possible sources of calcium, it represents a simple way of coupling calcium and voltage [42] and [30]. Unlike the other currents described so far, the extreme concentration gradient renders the Nernst approximation of the potential difference invalid. The proper derivation requires the use of the Goldman-Hodgkin-Katz equation [40] to get an equation for the driving potential

$$\Phi(v,c) = v\frac{1-(c/c_o)\exp(zv/V_T)}{1-\exp(zv/V_T)} \tag{2.20}$$

where c_o is the extracellular calcium concentrations, c is the intracellular calcium concentration, $z=2$ is the valence of calcium, and $V_T = 25.8$ mV at 27°C. Finally, depending on the type of calcium channel, there are several different gating models. The most biophysically accurate model we use is the L–type, Ca_L, calcium channel. The current associated with this channel can be described by the following first order kinetics

$$\begin{aligned} I_{Ca,L} &= g_{Ca,L}m_L^2\phi(v,c) \\ \tau_{m,L}m_L' &= m_{\infty,L}(v) - m_L \end{aligned} \tag{2.21}$$

However, in this work, we will also consider two simplified variants that approximate the L–type channel. First, we consider a model that has instantaneous activation. This model is derived from calcium channel models of the giant barnacle,

$$I_{Ca,ML} = g_{Ca} m_{\infty,ML}(v)\phi(v,c)\,. \tag{2.22}$$

The Morris-Lecar model of calcium current is distinguished by the fast activation of calcium [37]. This effectively strongly couples the calcium system to the voltage dynamics allowing the observed fluorescence time scale to more closely match the underlying voltage time scale.

Instead of approximating the speed of activation by eliminating the time delay in the gating equation, $\tau_{ML}(v) \equiv 0$, we could instead choose to use the heavy-side function instead of $m_{\infty,ML}$. Then we get the following model

$$\begin{aligned} I_{Ca,H} &= g_{Ca,H} m_H \phi(v,c) \\ \tau_{m,H}(v) m'_H &= \mathcal{H}(v) - m_H \end{aligned} \tag{2.23}$$

where now the voltage threshold of activation for the gating variable is instantaneous.

Chapter 3

Four inverse problems

3.1 Introduction

Recalling chapter 1, we wish to use fluorescence data from calcium imaging to ascertain channel densities. Although no work has been done to attack this problem directly, there have been several different approaches to both calcium recovery from imaging data and recovery of channel densities from voltage data. Our own approach will formulate and solve four interrelated inverse problems that will connect fluorescence data with calcium and potassium channel densities. The four inverse problems also parallel the three different experimental procedures that will slowly peel away the layers of equations that separate fluorescence from channel densities. We shall discuss some of the previous approaches to solving the individual inverse problems. Then, we shall discuss the experiment and the fluorescent data it generates. This will build some intuition about how to use the calcium imaging to infer channel densities. Then we shall review the four proposed inverse problems.

3.2 Related inverse problems

The recovery of calcium dynamics has been approached in a variety of ways. Biologically, Friel and collaborators [21] have been using careful experiments designed to measure the various calcium currents in the cell. This information has been incorporated into a model that describes how these currents are activated during cell depolarization [55]. From localized fluorescence data, Neher and collaborators have developed several techniques that can recover bounds on the diffusive and kinetic parameters of calcium and its buffer [52], [71],[51], [22], [69], [50], [53] under a simplifying assumption on the calcium system equations [38]. Additionally, under more controlled *in vitro* experiments, Naraghi [49] has measured the kinetics of several calcium indicators that have been widely used in subsequent fluorescence literature. Finally, recent theoretical work [5] and [48] have attempted to invert fluorescence time course data arising from single compartment cells to find the calcium time course.

The algorithmic approach to determining channel densities from voltage data has been proposed in several different settings. Each approach is tailored to a particular type of experimental data. From the micropipette based experiments, the experimentalist has access to either single or possibly dual potential recording. In the single recording setting, one particular approach has been to correct for axial currents during voltage-clamp experiments in order to deduce the local potassium conductance. Following [43], Schaefer et al. [59] proposed using a parameter driven simulation fitted to measured voltage data to determine the potassium conductance. The algorithm required knowledge of the cell's morphology and passive parameters. They then applied their technique to determine changes in the potassium conductance of neocortical neurons of layer 5B [60]. Cox [14] proposed the use of Cole's Theorem to solve for the potassium conductance. This approach significantly reduced the computational cost versus the Schaefer et al. algorithm.

With the advent of dual potential recordings, it became possible to develop methods to determine spatially distributed conductance information. Bell and Cracium [3]

proposed using a finite differencing scheme from spatially distributed potential recordings to recover channel densities. Cox [13] proposed using dual potential recordings within a least-squares framework to infer the hyperpolarizing cation channel densities. This extended the parameter fitting through least-squares of Schaefer et al. [59] by implementing analytic gradient computations. More recently, He and Keyes [26] have extended descent based least-squares approach to parameter identification problems in the Fitz-Nagumo equation.

3.3 Calcium fluorescence data

In general, the above approaches to the problem have been inadequate in determining channel densities throughout the dendritic tree. The problem is that local information about the cell at one or two places is not enough to determine the channel densities everywhere else. With the advent of acousto-optic deflector (AOD) based two-photon microscopy, experimentalists can now measure fluorescence at any point in the field of view and gather spatially distributed data. Therefore, we would like to recover the channel densities important in synaptic integration from this fluorescence data.

Figure 3.1 illustrates the distributed nature of the data from the AOD based microscopy. Time course fluorescence can be measured at different points on the geometry of the dendrites. Figure 3.1 also illustrates the difficulty of recovering information from fluorescence data. This data was gathered by applying current injection at the soma and monitoring the fluorescence changes throughout the dendrites under two different conditions. The gray traces represent the fluorescence change in the presence of a potassium channel inhibitor while the white trace is a control. The strong change in fluorescence for both traces indicates a large fast influx of calcium followed by a slower decay to rest. We do not know the exact amount of calcium since the fluorescence change is really measuring the amount of calcium bound buffer. The actual calcium flux depends on the characteristics of the buffer and its associated

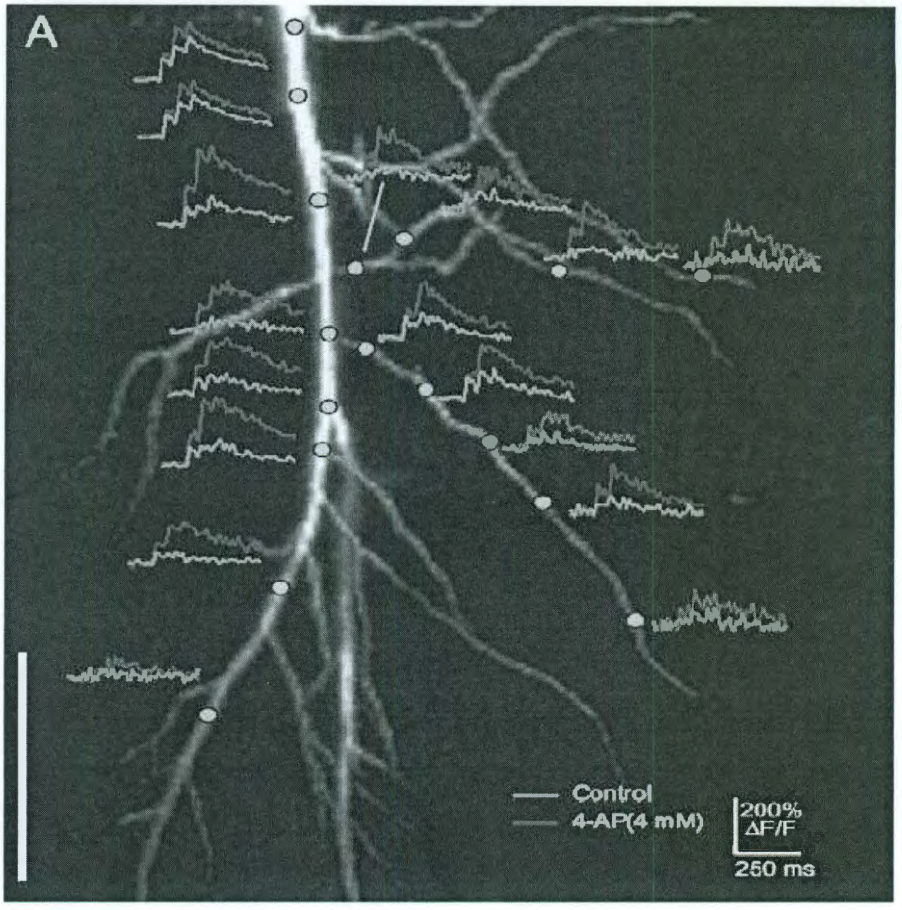

Figure 3.1: This image illustrates the temporal and spatial characteristics of the experimental data.The measured fluorescence from an experimental protocol carried out in Dr. Peter Saggau's Lab, Baylor College of Medicine, is shown on the neuron geometry. Under two different experimental conditions, the resulting time series data is plotted on the point at which is was measured [34].

kinetics, k_p and k_m in (2.12) as well as the local channel density at the recording site. Previous experimental work has shown that calcium flux will generally occur at depolarized voltage levels seen during action potential propagation. Therefore, we can infer the presence of a back propagating action potential induced by the current injection at the soma. An interesting trend in figure 3.1 is attenuation of the fluorescence signal farther away from the soma. Here, the difference between the two traces is a qualitative indication of the density of potassium channels. For example, where there is a large difference between the gray and white traces, that difference must be due to potassium channels. The blocking of potassium channel will cause the neuron to stay depolarized for a longer time. This allows more calcium flux into the cell and a larger change in fluorescence levels. Larger differences between the two traces indicates where there a higher potassium channel density relative to location with little difference between the two traces. This brief analysis shows how calcium imaging should be able to recover useful information about neuron channel densities.

3.4 The overall inverse problem

We now make the inverse problems we wish to solve concrete. From (2.1) and (2.12), we have a set of nonlinear parabolic equations that describes the responses of calcium, its buffer and the voltage in a neuron to a current injection. We have the ability to measure the amount of calcium bound buffer by way of fluorescence changes. By following the qualitative analysis of figure 3.1, we can deconstruct the four inverse problems we wish to solve. First, we need to understand how to convert calcium bound buffer concentrations, b, to calcium currents. This is not possible until we can determine the passive calcium parameters, $\{k_p, k_m, r\}$, in (2.12). Our approach will be to construct a separate experiment from the one described in figure 3.1 that will isolate the calcium-buffer system from the voltage system and other calcium systems in the neuron. In this experiment, we will introduce a controlled perturbation of

calcium and infer the passive calcium parameters from the moments of the calcium bound buffer data. Once we have these parameters, we construct an experimental setup similar to figure 3.1 and invert calcium bound buffer to recover the calcium current by directly solving for the current in (2.12) through numerical differentiation. In the third inverse problem, we take specific calcium channel models that relate calcium conductance and voltage to calcium current to invert Ohm's Law. Finally, in the fourth inverse problem, we use the recovered voltage data from the calcium current to back out the potassium channel densities. This last inverse problem is solved through a least-squares approach.

3.5 Recovery of calcium kinetics

The forward and backward reaction rates associated with the buffer, k_p and k_m, as well as the passive pump rate, r in the calcium-buffer system are part of the passive calcium properties of the neuron. These parameters describe the fluorescent response of the calcium–buffer system to voltage sensitive calcium channel, and their values must be known before inverting to get the calcium current. We simplify the recovery of the passive calcium parameters by decoupling them from the voltage dynamics through a separate experiment.

In the following experimental setup, a small fiber is filled with known quantities of Ca buffer, $\mathcal{B}$, and caged Ca through a micropipette. The neuron is allowed to sit for an adequate length of time so that the pipette and cytoplasmic concentrations equilibrate. The caged Ca blocks Ca from interacting with the cytoplasmic milieu. Then, upon flash photolysis by a pulse of UV laser, a few femtoliters of caged Ca are freed to diffuse and interact with the Ca buffer and neuronal pumps. The resulting reaction of the Ca buffer with Ca evokes a fluorescent signal, $\mathcal{F}$, that is measured by a second laser at every place on the fiber. Since only a small bolus of Ca is released, only the passive Ca pumps are active, and the resulting fluorescence is transient with exponential decay.

The equations describing the response of the calcium–buffer system is similar to (2.12) except the source of calcium is caged calcium. The caged compound releases calcium upon flash photolysis by UV light. This is preferable to voltage sensitive calcium because we have much more control over the behavior of the caged calcium. Since calcium is highly regulated, a large release triggers much more than the passive calcium machinery. This would significantly complicate the recover of the passive calcium parameters. The caged calcium allows us to introduce a small perturbation of calcium that will only engage the passive machinery. The response of calcium, c, and calcium bound buffer, b, in a small fiber of length, l, and radius, a, to perturbation

of caged calcium is give by

$$\begin{aligned}\partial_t b &= \partial_{xx} b + k_p c(\mathcal{B} - b) - k_m b \\ \partial_t c &= \partial_{xx} c - k_p c(\mathcal{B} - b) + k_m c - r(c - c_0) + u f(t)\delta(x - x_0)\end{aligned} \tag{3.1}$$

where k_p and k_m are the forward and backward reaction rates, D_b and D_c are the diffusivites of calcium and the calcium bound buffer, $\mathcal{B}$ is the total buffer concentration, r is the passive pump that maintains an intracellular concentration of c_0, u is the strength of uncaging, $f(t)$ is the associated time course specific to the type of calcium cage and x_0 is the location of uncaging. (3.1) differs from (2.12) in that source of calcium is now from an uncaging compound and not voltage sensitive calcium channels. Since we first allow the buffer time to equilibrate in the cytoplasm, (3.1) satisfies the following initial conditions

$$c(x,0) = c_0 \quad b(x,0) = \frac{\mathcal{B} c_0}{K_d + c_0} \tag{3.2}$$

and no flux boundary conditions

$$\partial_x c(0,t) = \partial_x c(l,t) = \partial_x b(0,t) = \partial_x b(l,t) = 0\,. \tag{3.3}$$

Experimentally, only the caged Ca concentrations, total buffer concentrations, $\mathcal{B}$, the dissociation constant, K_d, associated with the buffer reaction, the resting intracellular calcium concentration, c_0, and the time course of uncaging, $f(t)$, is known to us. Due to variability in the UV laser intensity and scattering by the tissue, the strength, u, of uncaging is not known. To convert fluorescence data to Ca bound buffer concentrations, we use the following formula

$$b(x,t) = \mathcal{B}\frac{\mathcal{F}(x,t) - \mathcal{F}_{min}}{\mathcal{F}_{max} - \mathcal{F}_{min}}\,. \tag{3.4}$$

where $\mathcal{F}_{min}$ and $\mathcal{F}_{max}$ are the absolute minimal and maximal observed fluorescence. In this problem, we wish to recover the scalar parameters $\{k_p,\ k_m,\ r,\ u\}$ from knowledge of $b(x,t)$ for $0 \le x \le l$ and $0 \le t \le T$.

Experimentally, the total amount of calcium released by uncaging perturbs calcium transiently from rest. Therefore from this rest state, we suppose the small pulse of UV laser, $\varepsilon u f(t)$, leads to the perturbations

$$b = b_0 + \varepsilon\tilde{b} \quad \text{and} \quad c = c_0 + \varepsilon\tilde{c} \tag{3.5}$$

where $b_0 \equiv b(x,0)$ and $c_0 \equiv c(x,0)$. After substitution of the perturbations into (2.12) and ignoring higher orders terms of ε, we see that $\tilde{b}$ and $\tilde{c}$ obey

$$\begin{aligned} \partial_t\tilde{b} &= D_b\partial_{xx}\tilde{b} + \beta\tilde{c} - \alpha\tilde{b} \\ \partial_t\tilde{c} &= D_c\partial_{xx}\tilde{c} - \beta\tilde{c} + \alpha\tilde{b} - r\tilde{c} + uf(t)\delta(x - x_c) \end{aligned} \tag{3.6}$$

where $\alpha = k_p c_0 + k_m$ and $\beta = k_p(\mathcal{B} - b_0)$. The perturbations satisfy the boundary conditions,

$$\partial_x\tilde{b}(0,t) = \partial_x\tilde{b}(l,t) = \partial_x\tilde{c}(0,t) = \partial_x\tilde{c}(l,t) = 0 \tag{3.7}$$

and the initial conditions, $\tilde{b}(x,0) = \tilde{c}(x,0) = 0$.

We proceed to uncover our parameters of interest by taking spatial averages of $\tilde{b}$ and $\tilde{c}$

$$B(t) = \int_0^l \tilde{b}(x,t)\,dx \quad \text{and} \quad C(t) = \int_0^l \tilde{c}(x,t)\,dx \tag{3.8}$$

and observe that they obey the following upon substitution into (3.6)

$$\begin{aligned} B'(t) &= \beta C(t) - \alpha B(t) \\ C'(t) &= -\beta C(t) - \alpha B(t) - rC(t) + uf(t) \end{aligned} \tag{3.9}$$

noting that (3.9) exhibits exponential decay for physiological parameter ranges. This approach eliminates the effect of the diffusion constants $\{D_b, D_c\}$ in the recovery of the kinetic parameters. Now, if we define the higher moments of B and C by

$$B_n \equiv \int_0^\infty t^n B(t)\,dt \quad \text{and} \quad C_n \equiv \int_0^\infty t^n C(t)\,dt \tag{3.10}$$

then we can get the following relationships

$$\beta\int_0^\infty C(t)\,dt - \alpha\int_0^\infty B(t)\,dt = \int_0^\infty B'(t)\,dt$$

which simplifies to

$$\beta C_0 - \alpha B_0 = 0 \tag{3.11}$$

after applying the fact that $B(t) \rightarrow 0$ as $t \rightarrow \{0, \infty\}$. Similarly we get the following equation for C

$$-\beta C_0 + \alpha B_0 - rC_0 + uf_0 = 0\,. \tag{3.12}$$

With one higher moment, we get

$$\int_0^\infty tB'(t)\,dt = \beta \int_0^\infty tC(t)\,dt - \alpha \int_0^\infty tB(t)\,dt \tag{3.13}$$

which we can simplify using integration by parts

$$\begin{aligned} tB(t)|_{t=0}^{\infty} - \int_0^\infty B(t)\,dt &= \beta C_1 - \alpha B_1 \\ -B_0 &= \beta C_1 - \alpha B_1 \end{aligned} \tag{3.14}$$

and similarly for C, we get

$$-C_0 = -\beta C_1 + \alpha B_1 - rC_1 + uf_1\,. \tag{3.15}$$

We add (3.11) and (3.12) to relate u in terms of r and the known strengths of the source, f_0, and response, B_0,

$$u = rC_0/f_0 = r\alpha B_0/(\beta f_0) \tag{3.16}$$

where we note the ratio,

$$\alpha/\beta = \frac{k_p c_0 + k_m}{k_p(\mathcal{B} - b_0)} = \frac{c_0 + K_d}{\mathcal{B} - b_0} = \frac{K_d \mathcal{B}}{(\mathcal{B} - b_0)^2} \tag{3.17}$$

is an *a priori* known quantity. Now, we add (3.14) and (3.15) and substitute (3.16) to get

$$r = 1 + \frac{\beta/\alpha}{B_1/B_0 + f_1/f_0 - 1/\alpha} \tag{3.18}$$

where again we can calculate the centroids of the source, f_1/f_0, and response, B_1/B_0. This leaves two unknown quantities in (3.18), α and r. If we recall that $\beta = k_p(\mathcal{B} - b_0)$,

running our experiment under two different total buffer concentrations gives us two equations from (3.18). This yields two equations to solve for α and r. If we let superscripts denote the experiment where 1 corresponds to $\mathcal{B} = 20$ μM and 2 with $\mathcal{B} = 80$ μM, then we can solve for α by

$$\alpha = \frac{\gamma_1 - \gamma_2}{\gamma_1(B_1^1/B_0^1 + f_1/f_0) - \gamma_2(B_1^2/B_0^2 + f_1/f_0)} \quad \gamma_i = \frac{\beta^i}{\alpha}. \tag{3.19}$$

To test this approach, we simulated the full nonlinear system, (2.12), under two different total buffer concentrations, $\mathcal{B} = 20$ μM and $\mathcal{B} = 80$ μM. Next, Gaussian noise with mean 0 and standard deviation of 5 nM was added to the data independently three times and averaged, $\langle b(x,t) \rangle$. The spatial averages, $B(t)$, were calculated by numerical integration of $\langle b(x,t) \rangle$. However, the averaged data contained too much noise to accurately calculate the strength and centroids. Therefore, exponentials were fit to the spatial averages before the strength and centroid of B were calculated. In figure 3.2(a), the spatially averaged data, $B(t)$, is plotted under the two different experimental $\mathcal{B}$ conditions. Each experiment yielded a line corresponding to (3.18). The crossing of the two lines from each experiment corresponds to the solution for α and r as shown in figure 3.2(b). Knowledge of r immediately gives us the parameter u through (3.16). Furthermore from (3.17), we see that

$$\beta = \frac{(\mathcal{B} - b_0)^2}{K_d \mathcal{B}} \alpha. \tag{3.20}$$

With knowledge of α and β, we can recover k_p and k_m using the following identities

$$k_p = \frac{\alpha}{c_0 + K_d}, \quad k_m = K_d k_p. \tag{3.21}$$

In the example in figure 3.2, this approach was able to recover the values of $r = 50.1$ and $\alpha = 340.3$ while the actual values were $r = 50$ and $\alpha = 310$.

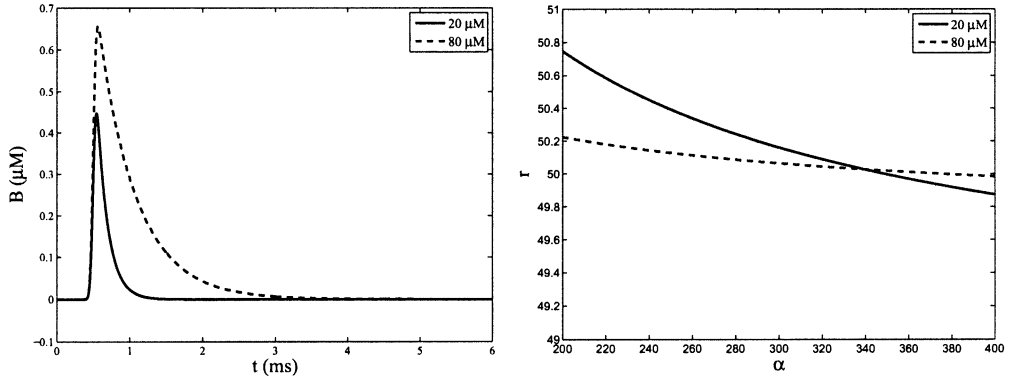

(a) The plot of the spatially averaged bound Ca signal, $B(t)$, under two different $\mathcal{B}$ concentrations, 20μM and 80μM.

(b) The intersection of the lines corresponding to two different total buffer concentrations, 20 and 80 μM respectively, reveal the pump rate, r, and kinetics, $\alpha = k_p c_0 + k_m$.

Figure 3.2: Recovery of the passive parameters of (2.12)

3.6 Recovery of the calcium current

With the passive properties of the Ca system in hand, we uncover the active mechanism. As in the previous experiment, a neuron from a slice of tissue will be interrogated with a micropipette that is filled with a Ca dye at the soma. We allow the patch and cytoplasm to equilibrate. A suprathreshold current is then applied at the soma to illicit an action potential. This depolarization causes voltage sensitive Ca channels to open and close in synchrony with the moving action potential as it travels through the dendritic tree. We are able to infer this behavior as the flux of Ca leads to fluorescence changes at recording sites along the dendritic tree. The response of calcium, c, and calcium bound buffer, b, to the voltage sensitive calcium current in a fiber of length l and radius a is give by

$$\partial_t b = D_b \partial_{xx} b - k_m b + k_p c(\mathcal{B} - b) \tag{3.22}$$

$$\partial_t c = D_c \partial_{xx} c + k_m b - k_p c(\mathcal{B} - b) - r(c - c_0) - I_{Ca}/(aF) \tag{3.23}$$

where D_b and D_c are the diffusion constants for calcium and calcium bound buffer, respectively. k_p and k_m are the forward and backward reaction rates. $\mathcal{B}$ is the total buffer concentration. r is the pump rate that keeps calcium at the intracellular resting level, c_0. I_{Ca} is the calcium current from voltage sensitive calcium channels.

Unlike the previous experiment, we are not considering a small patch of fiber. In figure 3.1, we see that over larger geometries, the microscopy technique is able to measure the time courses of fluorescence at relatively few points on the dendritic tree. We will show that the recovery of the calcium current can be done at each individual recording site.

Let $\{x_i\}_{i=1}^{B}$ be the points on the dendrites where can measure the fluorescence time course. Then, by converting fluorescence changes to calcium bound buffer concentrations through 3.4, We now ask whether knowledge of $b(x_i, t)$ at a point in the domain, x_i, from time $0 \leq t < T$ and the associated passive calcium parameters,

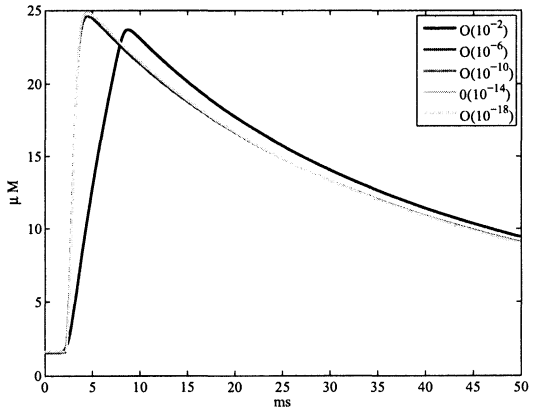

Figure 3.3: The solution of b from simulation of the coupled voltage and buffer equations is shown at a fixed point. Under physiological conditions, the diffusion constants of b and c are 10 orders smaller than the voltage equations. Therefore, there is no difference between the *in vivo* parameters and effectively zeroed diffusion of b and c. Conversely, it takes diffusion of a much larger magnitude to see an impact on the solution of b.

$\{k_p, k_m, r\}$, can determine $I_{Ca}(x_i, t)$. We first simplify (3.22) and (3.23) by assuming the diffusion constants, D_b and D_c, are zero. The result of approximating (3.22) and (3.23) without diffusion is shown in figure 3.6. We simulated the effect of magnitude changes on D_b and D_c in the presence of a fast moving action potential. As figure 3.6 illustrates, only when the diffusion constant of Ca and bound buffer increases by eight orders of magnitude from their physiological range is there any appreciable difference in the bound buffer time course. In figure 3.6, we see that setting the diffusion constants to zero still yields solutions to the calcium bound buffer that is accurate to four digits. The relative error used throughout this thesis to measure the accuracy of different assumptions and recovered parameters is calculated through

$$\text{relative error} = \frac{\|x-y\|_2}{\|x\|_2}, \quad \|x\|_2 = \sqrt{(x_1^2 + \cdots + x_n^2)} \text{ for } x \in \mathbb{R}^n. \tag{3.24}$$

By setting the diffusion constants to zero, we are effectively decoupling the spatial dependence of I_{Ca}. Therefore, we shall now confine ourselves to thinking of calcium current at fixed locations on the neuron and treat mathematically these objects in

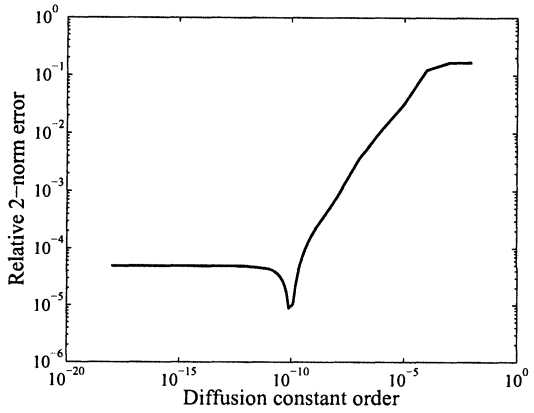

Figure 3.4: The diffusion constants for b and c are of order 10^-10 cm^2/ms. We varied the order of diffusion and measured the relative error 2–norm error of the original system. Assuming no diffusion of b and c yields 4 digits of accuracy.

time only. At the recording site, x_i, we set

$$I_{i,Ca}(t) \equiv I_{Ca}(x_i,t) \quad b_i(t) \equiv b(x_i,t) \quad c_i(t) \equiv c(x_i,t) \quad v_i(t) \equiv v(x_i,t) \quad g_{i,Ca} \equiv g_{Ca}(x_i)\,. \tag{3.25}$$

To solve for $I_{i,Ca}$, we proceed first to solve for c in (3.22). This yields

$$c_i = \frac{\partial_t b_i}{k_p(\mathcal{B}-b_i)} + \frac{K_d b_i}{\mathcal{B}-b_i} \tag{3.26}$$

which we substitute for c in (3.23) and solve for I_{Ca} to get

$$\begin{aligned} I_{i,Ca}/(aF) =& \partial_t c_i - k_m b_i + k_p c_i(\mathcal{B}-b_i) + r(c_i - c_0) \\ =& \frac{K_d \partial_t b_i}{(\mathcal{B}-b_i)^2} + \partial_t b_i + \frac{\partial_{tt} b_i}{k_p(\mathcal{B}-b_i)} + \frac{\partial_t b_i}{k_p(\mathcal{B}-b_i)^2} \\ & + r\left(\frac{\partial_t b_i}{k_p(\mathcal{B}-b_i)} + \frac{K_d b_i}{\mathcal{B}-b_i} - c_0\right)\,. \end{aligned} \tag{3.27}$$

By using (3.27) at each recording site, we can recover a spatially distributed set of time course currents, $\{I_{i,Ca}(t)\}_{i=1}^{B}$.

Experimentally, there is a large amount of noise in the fluorescence measurements. This noise is mitigated by running several experiments and averaging the data. The results as illustrated in figure 3.1 still contain too much noise to take two derivatives

of b_i in calculating $I_{i,Ca}$ from (3.27). Therefore, we shall fit a C^2 function via splines onto the averaged data to ensure sufficient regularity of twice differentiated data [25], [18]. Mathematically, we assume that data, $b_i(t)$, is gathered from n independently run trials and averaged to get $\langle b_i(t) \rangle$. We replace the average, $\langle b_i(t) \rangle$, with a spline smoothed version, $\phi_i(t)$, which solves the following equation

$$\begin{aligned} \min_{\phi \in C^2} \quad & \int_0^T |\phi''|^2 \, dt \\ s.t. \quad & \int_0^T |\phi(t) - \langle b_i(t) \rangle|^2 \, dt < \varepsilon \, . \end{aligned} \tag{3.28}$$

The spline is then substituted into (3.27) to solve for $I_{i,Ca}(t)$. Figure 3.5 illustrates the dependence of the choice of ε for the spline fit on the underlying noise added to the solution. We added Gaussian noise with zero mean and four different standard deviations, $\mathcal{N}(0, \sigma_i^2)$ where $\sigma = [0\, 0.01\, 0.05\, 0.01]$, to $b_i(t)$. We calculated the relative error in the approximations of b_i, $\partial_t b_i$ and $\partial_{tt} b_i$ with the spline function for the varying levels of noise. In figure 3.5(a), b_i and its derivatives for every level noise are plotted together. Looking at b_i, we see that approximation does not diverge for any value of ε. For $\partial_t b_i$, with no noise, we see the same behavior. However, as σ increases, denoted by darker lines, the value of ε at which the approximations diverge becomes larger. The behavior is repeated for $\partial_{tt} b_i$ with even larger values for ε where divergence is first seen. Figure 3.5(b) graphically illustrates the reason for this behavior. For fixed variance of $\sigma = 0.05$, the time series of the resulting spline approximation to the averaged calcium bound buffer data is shown with decreasing ε corresponding to lighter colors. When $\varepsilon = 10^{-8}$, the resulting regularity of the spline causes the difference approximations of the higher derivatives to accumulate large numerical errors. This is in contrast to $\varepsilon = 0.9$, whose derivatives do not diverge. Figure 3.5(a) shows how to choose ε for a given level of variance in the noise. The smallest possible ε provides the best approximation of $I_{i,Ca}$ when the spline function is substituted into (3.27). Figure 3.5(a) also shows that without additional averaging, the spline fitting procedure will fail for large variance in the experimental noise. For all numerical experiments, we

introduced the following four different noise profiles, $\sigma = [0\, 0.005\, 0.01\, 0.05]$ into the bound calcium buffer concentrations, b, and averaged 200 times.

Finally, we note an important qualitative consequences of the choice of ε on the recovery of the calcium current. In numerical experiments, ε could be chosen in two different ways. Smaller values of ε tend to capture the dynamics of perturbation from rest but would retain a larger noise characteristic at rest values. Larger ε values tended to smooth out any noise but would not fit perturbations from rest very well. However, they did tend to capture the points in time when the currents perturbed away from rest. The consequences of this behavior have important implications when recovering more information from the calcium current. Different approaches will require information of the current at different places and ε should be chosen accordingly. After many numerical experiments, we have found that $\varepsilon \approx \sigma^2/2$ results in an optimal spline fit of the noisy data.

3.7 Calcium conductance and voltage

With recovery of the calcium current, $\{I_{i,Ca}(t)\}_{i=1}^{B}$, and calcium concentrations, $\{c_i\}_{i=1}^{B}$, we proceed to use this data and invert Ohm's Law to recover the calcium conductance, $g_{i,Ca}$ and voltage, $v_i(t)$, at each recording site. Here, we must stop to consider experimental setup of our problem. One of the strengths of our approach to recovering I_{Ca} is that it is independent of the type and distribution of the channels underlying the calcium current. For instance, *in vivo* it is likely that some combination of L, T and N –type calcium channels are responsible for I_{Ca}. We will need now to make an additional assumption on our experimental setup. We will add all the necessary channel blockers so that only one particular type of calcium channel is active in our neuron. This is important because it allows us to stipulate the relationship between calcium conductance, voltage and calcium current.

We will consider three different channel models. In each of these models, we will

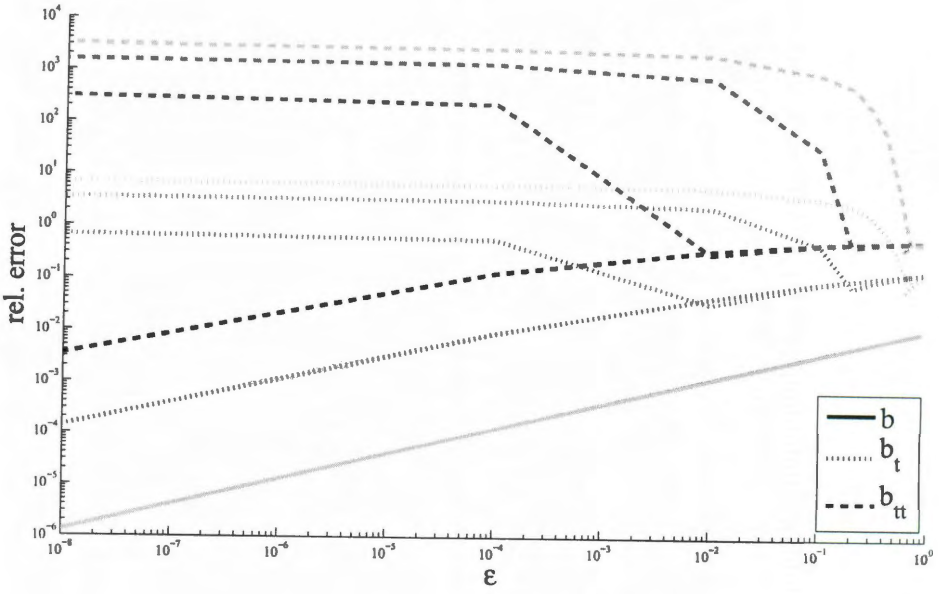

(a)

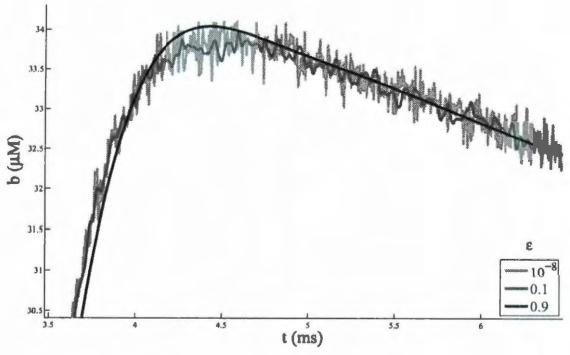

(b)

Figure 3.5: Fig. 3.5(a) illustrates the effect of σ, standard deviation, of the Gaussian noise with mean zero on the relative error in the spline fit to $\langle b_i \rangle$ and its first two time derivatives. The relative norm (y–axis) for a given ε value (x–axis) is shown. The darkest to lightest lines correspond to $\sigma = 0$, $\sigma = 0.01$, $\sigma = 0.05$ and $\sigma = 0.1$. Fig. 3.5(b), illustrates how the relative error quickly diverges for a given σ. In this case, $\sigma = 0.5$, the time-series plots of $\varepsilon = 0.9$, $\varepsilon = 0.1$ and $\varepsilon = 10^{-8}$ are superimposed on each other from darkest to lightest respectively.

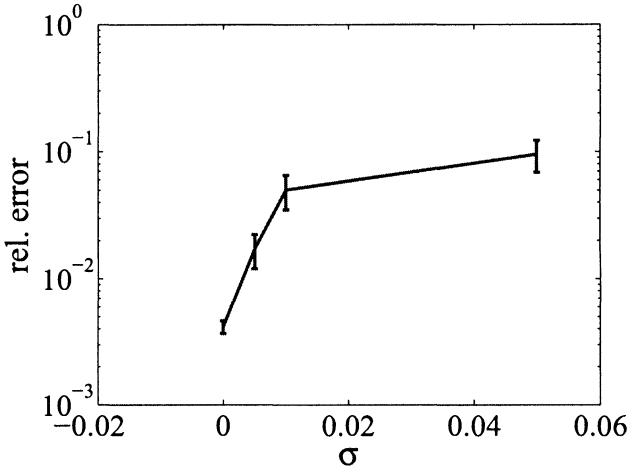

Figure 3.6: The mean and standard deviation of the relative error of the recovered calcium current is shown for four different noise profiles in the calcium bound buffer. Data was simulated from the full voltage–calcium system using random polynomials of degree ≤ 6 for g_{Ca}. Then Gaussian noise with mean zero and standard deviation, $\sigma = [0\ 0.005\ 0.01\ 0.05]$ μM was added to the calcium bound buffer before being averaged 200 times.

take derivatives of the calcium current to find points in time where the relationship between the current and voltage is independent of the conductance. At first, this may seem impossible given Ohm's law which requires both the conductance and voltage to stipulate the current. However, the conductance is really a function of voltage and only parametrized in time through voltage.

The key insight we shall use relies on the fact that regardless of how the functional voltage dependence of the current may be scaled, it has the same critical points. This underlies the idea of looking for critical points in the calcium current. At these points, the relationship between voltage and current is independent of the channel density. Experimental work has already determined the functional form of the voltage dependence of a single channel. We will look for critical points to determine how this functional dependence is scaled, i.e. the channel density.

We look at critical points of $I_{i,Ca}$ that arise from three different calcium channel models. The first model comes from studies of the calcium channels of the muscles

of barnacles. The calcium current for this channel is given by

$$I_{i,Ca,ML} = g_{i,Ca,ML} m_{\infty,ML}(v_i)\phi(v_i, c_i) \tag{3.29}$$

and is referred to as the Morris-Lecar channel model. This channel model tightly couples the voltage with the calcium current through $m_{\infty,ML}$. We rely on experimental evidence for the function form of $m_{\infty,ML}$. As a result, both v_i and $g_{i,Ca,ML}$ can be easily inferred from $I_{i,Ca,ML}$ and its critical points. This channel is not very accurate for neurons of the central nervous system in mammals. Usually, in neurons, there is a time delay in between voltage depolarization and channel activation. The usual convention for many channels is to assume that voltage-dependent conductance controlled by a gating variable satisfies the following differential equation

$$\tau_m(v)m' = m_{\infty,ML}(v_i) - m \tag{3.30}$$

which effectively delays and dampens the response to v_i. Therefore we introduce a second channel model that activates more slowly that the Morris-Lecar channel, but we now choose to approximate $m_{\infty,ML}$ by the heavy-side function to get

$$\begin{aligned} I_{i,Ca,H} &= g_{i,Ca,H} m_H \phi(v_i, c_i) \\ \tau(v_i)m'_H &= \mathcal{H}(v_i) - m_H \,. \end{aligned} \tag{3.31}$$

Finally, we shall work with an L–type calcium channel model that is seen throughout the mammalian central nervous system,

$$\begin{aligned} I_{i,Ca,L} &= g_{i,Ca,L} m_L \phi(v_i, c_i) \\ \tau_{m,L}(v_i)m'_L &= m_{\infty,L}(v_i) - m_L \end{aligned} \tag{3.32}$$

where the functional form of $m_{\infty,L}$ is known from prior experimental work. This last channel model is the most biophysically accurate but also the most challenging to recover voltage and calcium conductance from the calcium current.

Recover of $g_{Ca,ML}$ and v

Suppose the only type of unblocked channel in our neuron is the Morris-Lecar calcium channel. Ohm's Law state that the current at each recording site is prescribed by

$$I_{i,Ca,ML}(t) = g_{i,Ca,ML} m_{\infty,ML}(v_i(t))(v_i(t) - E_{Ca}) \tag{3.33}$$

where $g_{i,Ca}$ is the Ca conductance, $m_{\infty,ML}$ is the voltage dependent open channel probability and E_{Ca} is the reversal potential of the channel which approximates $\phi(v, c)$. Although this channel is not very biophysically accurate for the mammalian central nervous system, it is useful in illustrating one general approach to any channel model. Furthermore, as we shall soon discover, it has some very nice properties that allow for a robust recovery of $v_i(t)$. As such, we could view our results as an argument for inserting this invertebrate muscle channel in neurons as a voltage sensor. The inverse problem is to use the data $I_{i,Ca,ML}(t)$ knowledge of E_{Ca} and $m_{\infty,ML}$ from experiments to recover $g_{i,Ca,ML}$ and v_i. We first examine derivatives of $I_{i,Ca,ML}$. We note from

$$\partial_t I_{i,Ca,ML}(t) = g_{i,Ca,ML} \partial_t v_i(t)[m'_{\infty,ML}(v_i(t)))(v(t) - E_{Ca}) + m_{\infty,ML}(v_i(t)))] \tag{3.34}$$

the critical points of $I_{i,Ca,ML}$ are independent of $g_{i,Ca,ML}$, and for $v_i(t)$ in the physiological range, two of the three critical points occur at $\bar{v} = 16.85mV$. This idea is graphically illustrated in figure 3.7. Therefore, by finding the minima of $I_{i,Ca,ML}$ at $\bar{t}$, we can solve for $g_{i,Ca,ML}$ by substituting $\bar{t}$ and $\bar{v}$ into (3.33)

$$g_{i,Ca,ML} = \frac{I_{i,Ca,ML}(\bar{t})}{m_{\infty,ML}(\bar{v})(\bar{v} - E_{Ca})}. \tag{3.35}$$

Looking at derivatives of $I_{i,Ca}$ yields good information on v_i without knowledge of $g_{i,Ca,ML}$. Therefore, we shall extend this approach to a more accurate model whose potential is given by the Goldman-Hodgkin-Katz equation, $\phi(v, c)$ from (2.20). We can consider the more general case of the recovery of $g_{i,Ca,ML}$ and v_i from knowledge of $I_{i,Ca,ML}$, c_i and the function forms of $\{m_{\infty,ML}, h, \phi\}$ in

$$I_{i,Ca,ML} = g_{i,Ca,ML} m_{\infty,ML}(v_i) h_{ML}(c_i) \phi(v_i, c_i) \tag{3.36}$$

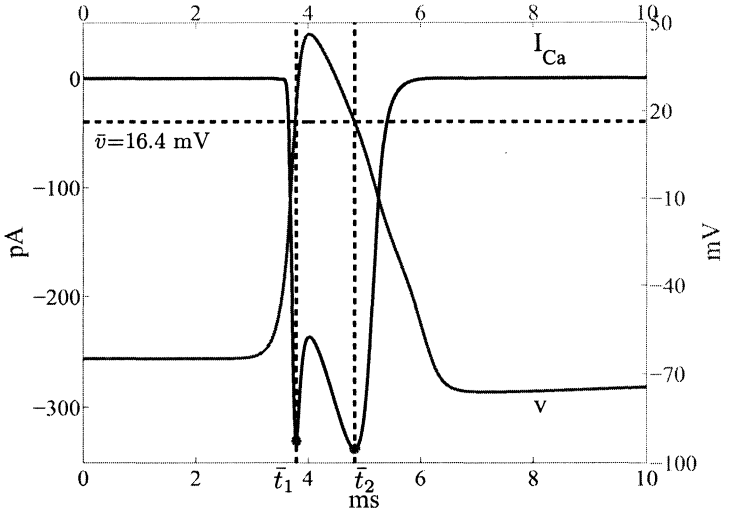

Figure 3.7: On a two different y axes, $I_{Ca,ML}$ and v are plotted to illustrate the relationship between critical points of $I_{Ca,ML}$ and v.

where $h_{ML}(c_i)$ is the calcium-dependent inactivating gating variable. We shall assume it has the following form

$$h_{ML}(c_i) = \frac{K_c}{K_c + c_i} \tag{3.37}$$

which initially allows calcium current into the cell before decreasing the current as calcium accumulates faster in the cytoplasm than it can be cleared by passive mechanisms. We proceed first to scale $I_{i,Ca,ML}$ by h_{ML}, $\hat{I}_{i,Ca,ML} \equiv I_{i,Ca,ML}/h_{ML}$ and differentiate it to get

$$\partial_t \hat{I}_{i,Ca,ML} = g_{i,Ca,ML}\left(m'_{\infty,ML}(v_i)\phi(v_i,c_i) + m_{\infty,ML}(v_i)\partial_v\phi(v_i,c_i)\right)\partial_t v_i + m_{\infty,ML}(v_i)\partial_c\phi(v_i,c_i)\partial_t c_i\,. \tag{3.38}$$

We use the data, $c_i(t)$, to solve for v_i through the equation

$$m'_{\infty,ML}(v_i)\phi(v_i,c_i) + m_{\infty,ML}\partial_v\phi(v_i,c_i) = 0 \tag{3.39}$$

which effectively parametrizes v_i as $v_i \equiv v(c_i)$. By doing so, we reduce the derivative of $\hat{I}_{i,Ca,ML}$ to the following

$$\partial_t \hat{I}_{i,Ca,ML}(t) = g_{i,Ca,ML} m_{\infty,ML}(v_i)\partial_c\phi(v_i,c_i)\partial_t c_i\,. \tag{3.40}$$

By multiplying both sides by data, $\phi(v(c_i), c_i)$, we get the following equation

$$\phi(v(c_i), c_i)\partial_t \hat{I}_{i,Ca,ML}(t) = I_{Ca,ML}(v(c_i), c_i)\partial_c \phi(v(c_i)), c_i)\partial_t c_i \,. \tag{3.41}$$

We therefore look for the triple $(\bar{t}, c_i(\bar{t}), v(c_i(\bar{t})))$ where (3.41) holds and use that to get

$$g_{i,Ca,ML} = \frac{I_{i,Ca,ML}(\bar{t})}{m_{\infty,ML}(v(c_i(\bar{t})))h_{ML}(c_i(\bar{t}))\phi(v(c_i(\bar{t})), c_i(\bar{t}))} \,. \tag{3.42}$$

With $g_{i,Ca}$ in hand, we return to (3.36) and note that it becomes a nonlinear equation in $v_i(t)$

$$I_{i,Ca,ML}(t) - g_{i,Ca,ML} m_\infty^{Ca}(v_i(t))\phi(v_i(t), c_i(t)) = 0 \tag{3.43}$$

and employ an optimization scheme to solve (3.43) for $v_i(t)$. To solve this problem, we discretize time, $t = [0, \tau, 2\tau, ..., (Nt-1)\tau = T]$, and define the voltage on this grid by $v_{i,j} \equiv v_i(\tau j)$. We then solve the following equation

$$\begin{aligned} \min_{v \in \mathbb{R}} \quad & [I_{i,Ca,ML}(t_j) - g_{i,Ca,ML} m_{\infty,ML}(v)\phi(v, c_i(t_j))]^2 \\ s.t. \quad & E_K \leq v \leq E_{Na} \end{aligned} \tag{3.44}$$

for $j = 0, .., Nt-1$. The constraints in (3.44) are due to the non-convexity of the objective function. In figure 3.8(a), the x-axis and y-axis are in ms and mV, respectively. This contour plot shows the value of the objective function in (3.44) for all t_j. The objective function contains three regions. The boundaries of these regions are delineated by the two values of $\{\bar{t}_1, \bar{t}_2\}$ corresponding to where v crosses 16.85 mV. We denote the regions I, II and III by $0 < t < \bar{t}_1$, $\bar{t}_1 < t < \bar{t}_2$ and $\bar{t}_2 < t < T$, respectively. Regions I and III have unique minimizers in $[E_K, E_{Na}]$, whereas region II does not. Moreover, due to the non-convexity of the objective function, the starting guess for the descent schemes in regions I and III must start from the left hand side of the interval, $[E_K, E_{Na}]$, for v. Otherwise, the descent scheme will not converge. However, in order to find the correct minimizer in region II, the starting guess must start from the right hand side of the interval, $[E_K, E_{Na}]$. This idea is shown in figure

3.8(b) where the plot of v and I_{Ca} are shown together. A sample of the objective function for each region is shown in plot insets in figure 3.8(b) with the correct minimizer shown with a circle. Noise in the data can cause error in the location of $\bar{t}$. In the process of finding $v_i(t)$, if the boundaries between the intervals are incorrect, the bounds in (3.44) keep the descent scheme from stalling. Finally, starting from the wrong side of the interval for v will result in the incorrect minimizer being chosen.

Recovery of $g_{Ca,H}$ and v

The assumptions made on the voltage sensitive calcium channel in (3.36) are unrealistic for mammalian neurons of the central nervous system. A better approximation would be to assume a time delay in the activation of Ca channels. We will instead approximate the voltage-dependent activation of the gating variable with the Heaviside function, $\mathcal{H}$. This results in the following equation for the associated calcium current, $I_{i,Ca,H}$,

$$\begin{aligned} I_{i,Ca,H} &= g_{i,Ca,H} m_H h(c_i)\phi(v_i, c_i) \\ \tau_{m,H}(v_i)\partial_t m_H &= \mathcal{H}(v_i) - m_H \,. \end{aligned} \tag{3.45}$$

Our previous approach to finding $g_{i,Ca,H}$ and v_i from $I_{i,Ca,H}$, c_i fails in this setting. The three critical points in figure 3.7 coalesce into one critical point. Therefore, we try a different approach to solve our inverse problem. In (3.45) we solve for m_H thinking of $\mathcal{H}$ as the source for a first-order linear ode to get

$$m_H(t) = \int_0^t \tau_{m,H}^{-1}(v_i(s))\mathcal{H}(v_i(s)) e^{-\int_s^t \tau_{m,H}^{-1}(v_i(z))\,dz}\, ds \,. \tag{3.46}$$

We then substitute (3.46) into $I_{i,Ca,H}$ to get the following equation

$$I_{i,Ca,H} = g_{i,Ca,H}\phi(v_i, c_i)h(c_i) \int_0^t \tau_{m,H}(v_i(s))\mathcal{H}(v_i(s)) e^{-\int_s^t \tau_{m,H}^{-1}(v_i(z))\,dz}\, ds \,. \tag{3.47}$$

If we let $v_i(t_0) = 0$ and $c_i(t_0) = c_0$, then we see from (3.47) that $I_{i,Ca,H}(t_0) = 0$ for $t \leq t_0$ because $m_H(t_0) = 0$ for $t \leq t_0$. We shall take the right-handed derivative of $I_{i,Ca,H}$ at t_0, $I'_{i,Ca,H}(t_0^+)$, to get

$$I'_{i,Ca,H}(t_0^+) = g_{i,Ca,H}(m'_H(t_0^+)\phi(0, c_0) + m_H(t_0^+)\phi'(0, c_0)) = g_{Ca}\phi(0, c_0)m'_H(t_0^+) \tag{3.48}$$

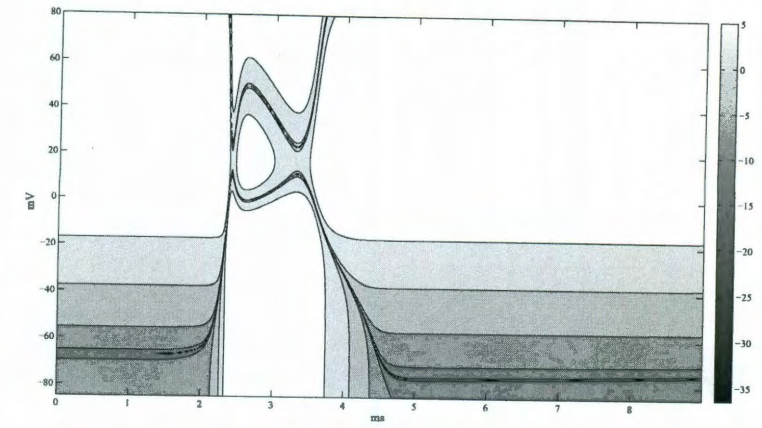

(a)

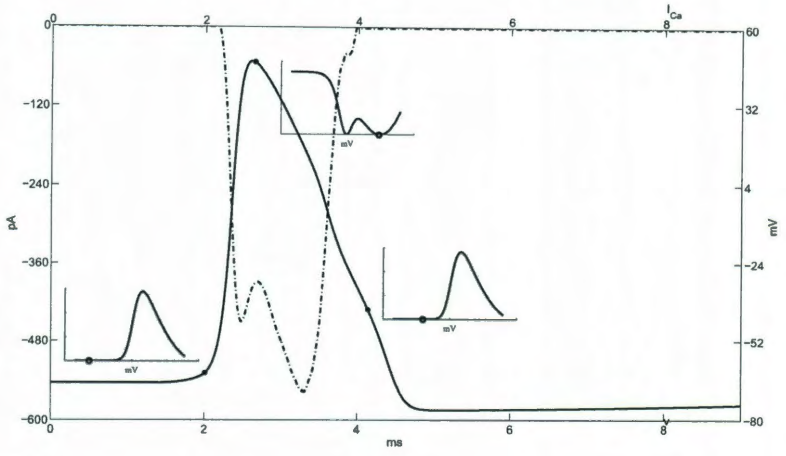

(b)

Figure 3.8: Fig. 3.8(a) shows the objective function for the nonlinear equation in v. The contour plot's values are plotted on the log scale. Close examination of the function shows the existence of three regions separated by times corresponding to inflection points in I_{Ca}. The first and third regions contain unique minimizer, whereas the second does not. Following the minimum along time yields the recovered waveform. Fig 3.8(b) shows the objective functions (insets) corresponding to the points plotted on the voltage line. Each point represents its region's objective function characteristic. The true v is shown on the inset x-axis with a circle.

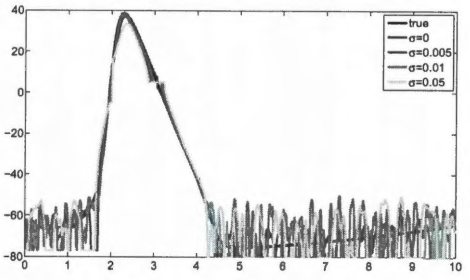

(a) Recovery of the voltage

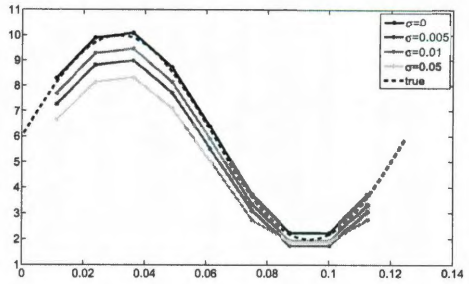

(b) Recovery of $g_{Ca,ML}$

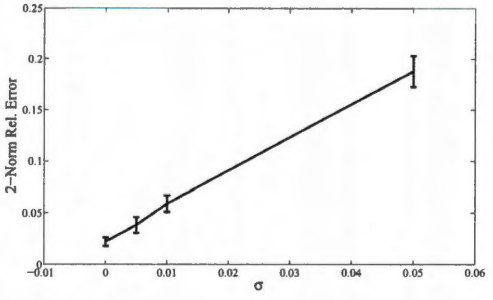

(c) Noise analysis for $g_{Ca,ML}$ recovery

Figure 3.9: The recovered voltage in 3.9(a) and calcium conductance 3.9(b) are plotted for the Morris-Lecar model under three different noise profiles in the calcium bound buffer. Gaussian noise with mean zero and standard deviation $\sigma = [0\ 0.005\ 0.01\ 0.05]$ μM was added to the calcium bound buffer and then averaged 200 times. The resulting recovery of voltage and conductance from the Morris-Lecar calcium channel model is shown where lighter lines correspond to higher variance in the added noise. 3.9(c) shows the mean and standard deviation of the relative error in $g_{Ca,ML}$ at each recording site from a set of random polynomials of degree ≤ 6.

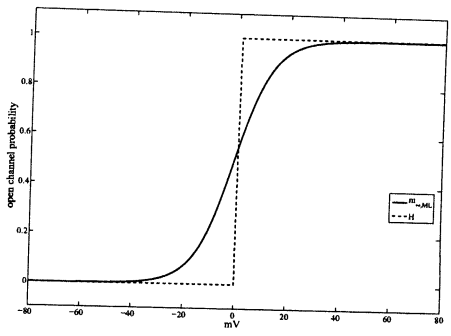

Figure 3.10: The approximation of $m_{\infty,ML}$ by the Heavy-side function, H, centered at $v = 0$ mV.

where we have used the fact that $m_H(t_0^+) = 0$. We note that $m'_H(t_0^+)$ has the following simple form

$$\begin{aligned} m'_H(t_0^+) &= \tau_{m,H}^{-1}(0) - \tau_{m,H}^{-1}(0) \int_0^{t_0^+} \tau_{m,H}(v(s))\mathcal{H}(v(s)) e^{-\int_s^{t_0^+} \tau_{m,H}^{-1}(v(z))\,dz}\,ds \\ &= \tau_{m,H}^{-1}(0) \end{aligned} \tag{3.49}$$

so that (3.48) reduces to

$$I'_{i,Ca,H}(t_0^+) = g_{i,Ca,H} \frac{\phi(0, c_0)}{\tau_{m,H}(0)} \tag{3.50}$$

which can be used to solve for $g_{i,Ca,H}$. Before we solve for $v_i(t)$, we note that when potassium channels turn on in response to the depolarization, there exists a $t_1 > t_0$ where $v(t_1) = 0$ as the voltage returns to rest as illustrated in figure 3.7. With $g_{i,Ca,H}$ and knowledge of t_0, we go back to (3.47) and solve for $v_i(t)\, t \geq t_0$ through the same nonlinear procedure we used in the Morris-Lecar calcium channel model. It is slightly more complicated because we can no longer solve for each time-discretized voltage, $v_{i,j}$, individually but must also keep track of the gating variable. If we let $m_{H,j} \equiv m_H(\tau j)$ and use backward Euler to discretize $m'_H(t)$, we get

$$m_{H,j} = \frac{\tau_m(v_{i,j}) m_{H,j-1} + \tau \mathcal{H}(v_{i,j})}{\tau_m(v_{i,j}) + \tau}. \tag{3.51}$$

We note that if $m_{H,j-1}$ is known, (3.51) relates $m_{H,j}$ to $v_{i,j}$. Let $\tau j_0 \approx t_0$, then we

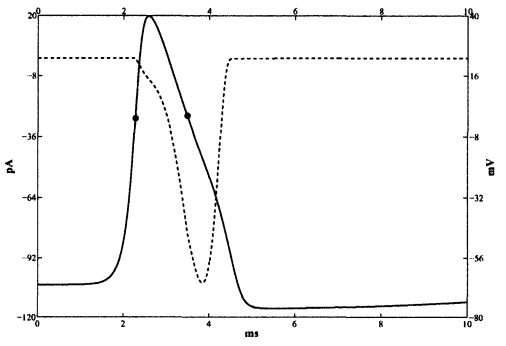

Figure 3.11: Voltage (lined) and $I_{i,Ca,H}$ (dotted) are plotted together to show the dependence of the current on the threshold voltage, 0 mV. Both $v(t_1)$ and $v(t_0)$ (dots) are shown to illustrate that the voltage crosses 0 mV twice during one action potential.

solve for $\{v_{i,j}\}_{j=j_0}^{Nt-1}$ iteratively through

$$\min_{v\in\mathbb{R}} \left[I_{i,Ca,H}(t_j) - g_{i,Ca,H} m_{H,j}(v)\phi(v, c_i(t_j))\right]^2 \tag{3.52}$$

where $v_{i,j_0} = 0$ and $m_{H,j_0} = 0$. Although we have relied on an approximation of $m_{\infty,ML}$ to solve for $g_{i,Ca,ML}$ and v_i, under certain experimental situations this may be an accurate approximation.

Recovery of $g_{Ca,L}$ and v

Unlike our previous two approaches, a more biophysically accurate calcium channel model requires a different experimental setup. In this experiment to recover L–type calcium channel densities, we require our same experiment to be run under two different extracellular calcium concentrations. We can view this change in extracellular calcium as a perturbation that will lead to changes in intracellular calcium and the corresponding calcium current. However, since calcium currents make up a relatively small part of the total current during action potential propagation, the perturbation should not lead to changes in the voltage. To confirm this hypothesis, we calculated the relative error between the simulated voltages under two different extracellular cal-

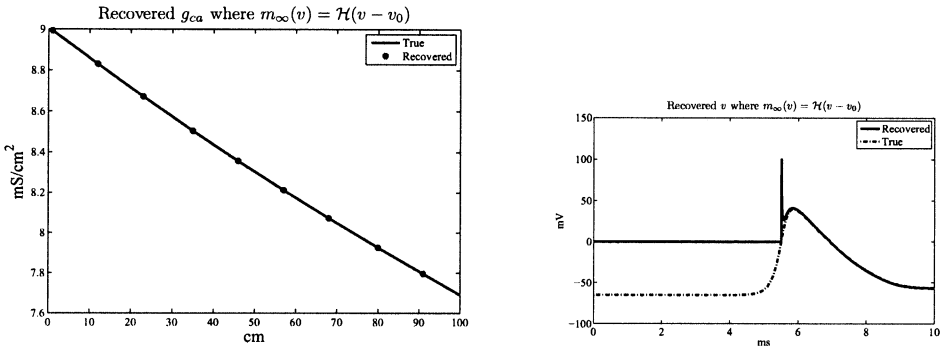

(a) Recovered $g_{i,Ca,H}$ (b) Recovered voltage

Figure 3.12: Recovery of the conductance and voltage from $I_{i,Ca,H}$ in the absence of noise.

cium concentrations under a range of constant g_K and g_{Ca} values. Figure 3.13 shows that as long as the calcium conductance stays below the potassium conductance, the two voltages agree to at least three digits. Therefore the ratio of the calcium currents from the two experiments, $I^1_{i,Ca}(t)$ and $I^2_{i,Ca}(t)$, should reveal information about v_i. With v_i in hand, we can then uncover $g_{i,Ca,L}$. In figure 3.14, the results of simulation show the effect of the extracellular calcium concentration on the buffer and current for two different values of the calcium conductance. Figure 3.14, seems to indicate that larger calcium conductances separate calcium currents. However, a two order magnitude difference in extracellular calcium seems to translate into a much smaller perturbation in current. This effect seems to be attributable to the calcium buffer. If we look back at the Goldman-Hodgkin-Katz potential function

$$\phi(v, c^{in}, c^{out}) = v\frac{1 - (c^{in}/c^{out})\exp(zv/V_T)}{1 - \exp(zv/V_T)}. \tag{3.53}$$

we can see that the ratio c^{in}/c^{out} determines the impact of calcium on potential. In the presence of large amounts of unbound buffer, c^{in} will never be large enough to impact the ratio c^{in}/c^{out} whether $c^{out} = 1000$ or 10 μM. One way of ensuring a larger intracellular calcium concentration is to lower the total buffer concentration. Figure 3.15 shows the effect of changes on $\mathcal{B}$ to the ratio of $I^1_{i,Ca,L}$ to $I^2_{i,Ca,L}$. The decrease in

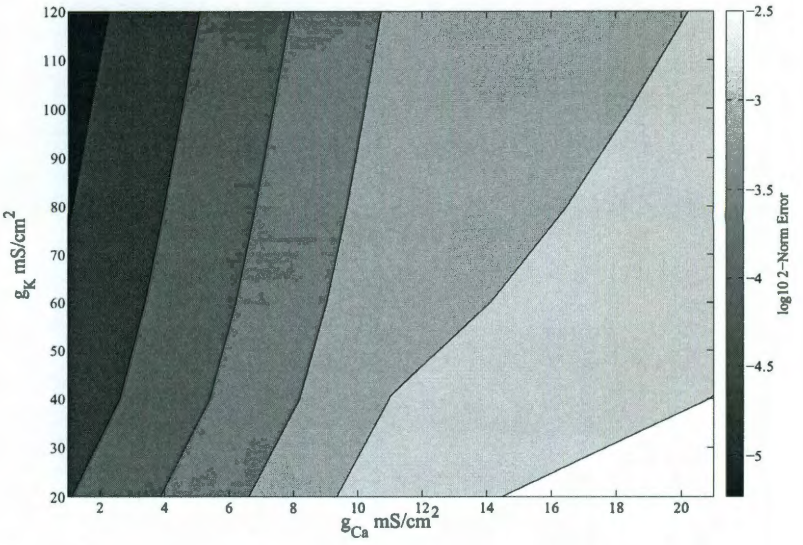

Figure 3.13: The relative error between the voltages under two different extracellular concentrations, 10μM and 1000μM respectively, were compared under a range of g_K and g_{Ca} values. In these simulation, the corresponding channel conductances were constant throughout the neuron.

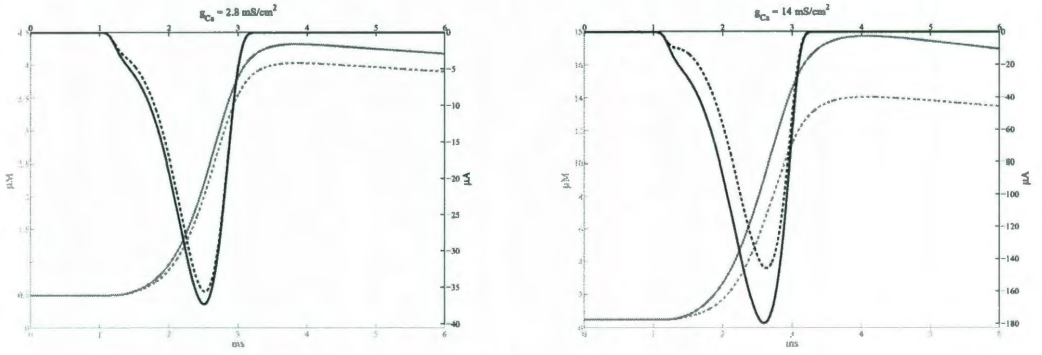

(a) $g_{Ca} = 2.8\text{mS/cm}^2$ (b) $g_{Ca} = 14\text{mS/cm}^2$

Figure 3.14: These two plots illustrate the effect of the calcium conductance in distinguishing the calcium buffer(gray) and current(black) time course under the two different extracellular calcium – $c^{out} = 1000\mu$M (lined) and $c^{out} = 10\mu$M (dotted). In both figures, we see the effect of the change in extracellular calcium concentrations on the buffer and current. The larger conductance value is able to separate both buffer and current than the smaller calcium conductance.

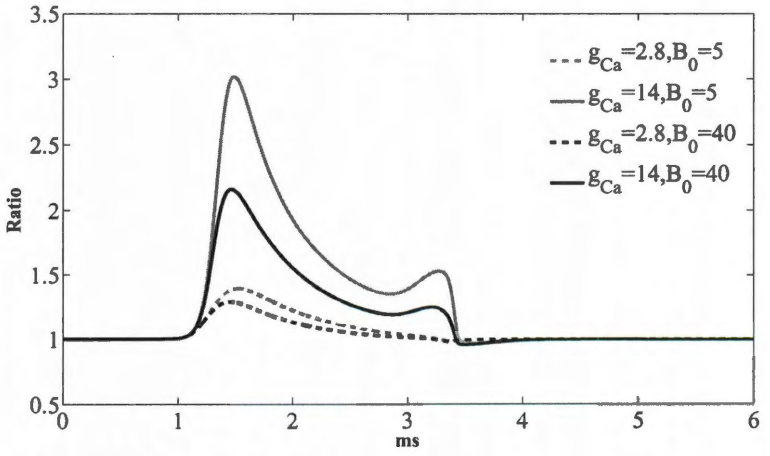

Figure 3.15: The ratio of $I_{i,Ca,L}$ for two different experiments, $c^{out} = 1000\mu$M and $c^{out} = 10\mu$M, respectively, are shown under four different parameter changes in g_{Ca} and $\mathcal{B}$. The calcium conductance has been changed to allow either larger or smaller amounts of intracellular calcium. As expected, under both $\mathcal{B}$ conditions, the larger conductance values gives a larger ration value. Under smaller $\mathcal{B}$ conditions, the ratio is much larger.

$\mathcal{B}$ corresponds to larger ratios. In our experiments, we shall set $\mathcal{B} = 10\mu$M.

In our experimental setup, we block T– and N–type calcium channels. Then, after stimulation of the neuron we recover the calcium current, $I^1_{i,Ca,L}$ with normal extracellular concentration (1000μM) and the intracellular calcium concentration, $c^{in}_{i,1}(t)$, at each recording site. Then we reduce the extracellular concentration to 10μM and recovery the calcium current, $I^2_{i,Ca,L}$, and the corresponding intracellular calcium concentration, $c^{in}_{i,2}(t)$. We recall that the L–type calcium current is prescribed by

$$\begin{aligned} I_{i,Ca,L} &= g_{i,Ca,L} m_L^2 \phi(v_i, c_i^{in}, c^{out}) \\ \tau_{m,L}(v_i) m_L' &= m_{\infty,L}(v_i) - m_L \,. \end{aligned} \tag{3.54}$$

We denote the extracellular and intracellular calcium concentration under normal conditions to be c^o_1 and $c^{in}_{i,1}$, respectively. Let the perturbation in extracellular calcium from the second experiment, c^{out}_2, leads to a corresponding change in intracellular calcium, $c^{in}_{i,2}$ but not a change in voltage, v_i, then the ratio of the recovered currents

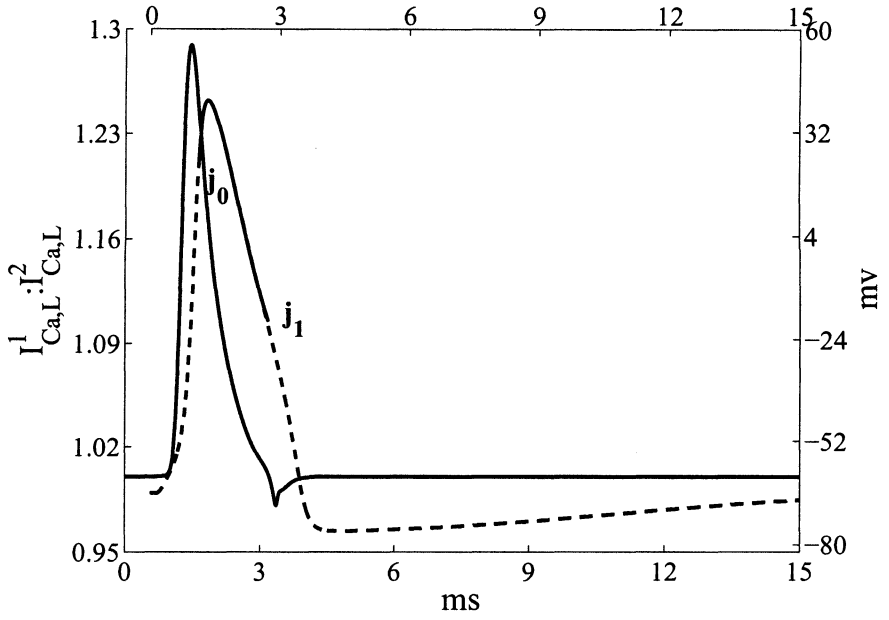

Figure 3.16: The ratio of $I^1_{Ca,L}$ to $I^2_{Ca,L}$ (lined) from $c_1^{out} = 1000$ μM and $c_2^{out} = 10$ μM is plotted. The actual voltage (dotted) and the recovered voltage, v_{rec} (lined on dotted), are also shown.

is

$$\frac{I^1_{i,Ca,L}}{I^2_{i,Ca,L}} = \frac{g_{i,Ca,L} m_L^2 \phi(v_i, c^{in}_{i,1}, c_1^{out})}{g_{Ca,L} m_L^2 \phi(v_i, c^{in}_{i,2}, c_2^{out})} = \frac{1 - (c^{in}_{i,1}/c_1^{out}) \exp(zv/V_T)}{1 - (c^{in}_{i,2}/c_2^{out}) \exp(zv/V_T)} . \tag{3.55}$$

From the ratio, we can solve for v_i

$$v_i = \frac{V_T}{z} \ln\left(\frac{R-1}{R(c^{in}_{i,2}/c_2^{out}) - (c^{in}_{i,1}/c_1^{out})}\right), \quad R = \frac{I^1_{i,Ca,L}}{I^2_{i,Ca,L}} . \tag{3.56}$$

We note from figure 3.16 that (3.56) is only useful when $R \neq 1$. Therefore, this approach reveals only partial voltage information. However, with this voltage information, we still can not recover $g_{i,Ca,L}$ since the gating variable is unknown. We consider two approaches to finding the value of m_L so that we can solve for $g_{i,Ca,L}$. In

the first approach, we look at critical points of $I^1_{i,Ca,L}$. When we differentiate $I^1_{i,Ca,L}$,

$$\begin{aligned} I^{1'}_{i,Ca,L} &= g_{i,Ca,L}\left(2m'_L m_L \phi(v_i, c^{in}_{i,1}) + m_L \phi'(v_i, c^{in}_{i,1})\right) \\ &= g_{i,Ca,L}\left(2\frac{m_{\infty,L}(v_i) - m_L}{\tau_{m,L}(v_i)} m_L \phi(v_i, c^{in}_{i,1}) + m_L \phi'(v_i, c^{in}_{i,1})\right) \\ &= g_{i,Ca,L}\tau_{m,L}(v_i) m_L \left(2m_{\infty,L}(v_i)\phi(v_i, c^{in}_{i,1}) - (\phi(v_i, c^{in}_{i,1}) - \phi'(v_i, c^{in}_{i,1})\tau_{m,L}(v_i))m_L\right), \end{aligned} \tag{3.57}$$

we see that for $I^{1'}_{i,Ca,L}(t_1) = 0$ implies that

$$m_L(t_1) = \frac{2m_{\infty,L}(v_i(t_1))\phi(v_i(t_1), c^{in}_{i,1}(t_1))}{\phi(v_i(t_1), c^{in}_{i,1}(t_1)) - \phi'(v_i(t_1), c^{in}_{i,1}(t_1))\tau_{m,L}(v_i(t_1))}. \tag{3.58}$$

Therefore, we can solve for $g_{i,Ca,L}$ by

$$g_{i,Ca,L} = \frac{I^1_{i,Ca,L}(t_1)}{m_L(t_1)^2 \phi(v_i(t_1), c^{in}_{i,1}(t_1))} \quad t_1 = \underset{t}{\operatorname{argmin}}\, I_{Ca}(t). \tag{3.59}$$

Alternatively, we can look for critical points of m_L. Let $m'_L(t_2) = 0$, then

$$I^{1'}_{i,Ca,L}(t_2) = g_{i,Ca,L} m_L(t_2)^2 \phi'(v_i(t_2), c^{in}_{i,1}(t_2)) \tag{3.60}$$

which gives us the following relation when we multiply through by $\phi(v_i(t_2), c^{in}_{i,1}(t_2))$

$$\phi(v_i(t_2), c^{in}_{i,1}(t_2)) I^{1'}_{i,Ca,L}(t_2) = I^1_{i,Ca,L}(t_2)\phi'(v_i(t_2), c^{in}_{i,1}(t_2)). \tag{3.61}$$

By finding t_2 that satisfies this relationship, we know that $m_L(t_2) = m_{\infty,L}(t_2)$ and

$$g_{i,Ca,L} = \frac{I^1_{i,Ca,L}(t_2)}{m_{\infty,L}(v_i(t_2))^2 \phi(v_i(t_2), c^{in}_{i,1}(t_2))}. \tag{3.62}$$

These two points and their associated relationship to m_L and $I_{i,Ca,L}$ are shown in figure 3.17. Once we have solved for $g_{i,Ca,L}$, we can go back and solve for $v_i(t)$ through an iterative procedure similar to (3.52). From (3.56), we solve for $\{v_{i,j}\}_{j=j_0}^{j_1}$ corresponding to where $R > 1$ and $\{m_{L,j}\}_{j=j_0}^{j_1}$ by integrating forward and backward in time from either t_1 or t_2. Once we have recovered v_i and m_L where $R > 1$, we proceed to solve for $v_{i,j}$ outside of this interval through the iterative solution to the

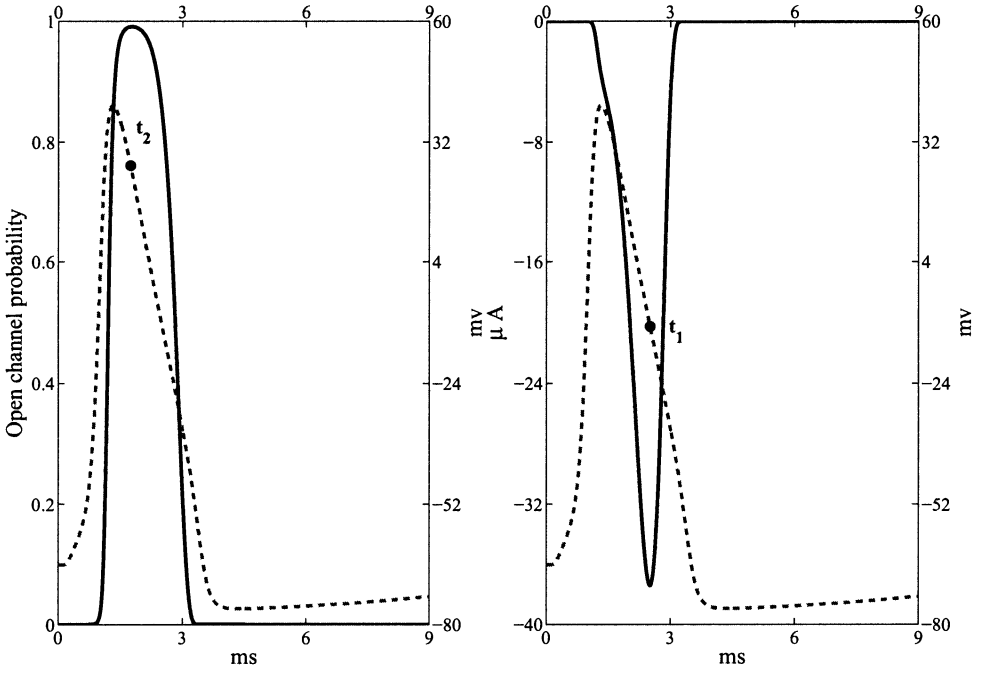

Figure 3.17: The location of t_1 and t_2 are shown to graphically illustrate their dependence on critical points of $I_{i,Ca,L}$ and m_L, respectively.

following equations, similar to (3.52). For $j < j_0$, we march backwards in time by iterating

$$m_{L,j}(v_{i,j}) = \frac{\tau_m(v_{i,j})m_{L,j+1} - \tau m_{\infty,L}(v_{i,j})}{\tau_m(v_{i,j}) - \tau} \tag{3.63}$$

and $v_{i,j}$ solves

$$\min_{v\in\mathbb{R}} \sum_{n=1}^{2} \left[I^n_{i,Ca,L}(t_j) - g_{i,Ca,L}m_{L,j}(v_j)\phi(v_j, c^{in}_{i,n}(t_j))\right]^2 \tag{3.64}$$

from the terminal condition data (v_{i,j_0}, m_{L,j_0}). For $j > j_1$, we march forward in time by iterating

$$m_{L,j}(v_{i,j}) = \frac{\tau_m(v_{i,j})m_{L,j+1} + \tau m_{\infty,L}(v_{i,j})}{\tau_m(v_{i,j}) + \tau} \tag{3.65}$$

and $v_{i,j}$ solves

$$\min_{v} \sum_{n=1}^{2} \left[I^i_{i,Ca,L}(t_j) - g_{i,Ca,L}m_{L,j}(v_j)\phi(v_j, c^{in}_{i,n}(t_j))\right]^2 \tag{3.66}$$

from the initial condition (v_{i,j_1}, m_{L,j_1}).

The recovery of the voltage and calcium conductance is shown in figure 3.19 and 3.18 from data generated in the absence of any noise in the calcium bound buffer. In order to test the robustness the recovery of $g_{i,Ca,L}$, we generated calcium bound buffer concentrations from channel densities drawn from random polynomials. Different levels of noise were added to the buffer concentrations before averaging. Figure 3.20 illustrates the effect of the noise on the relative error of the recovered conductance at the recording sites on the neuron. The recovery is able to take $I_{i,Ca}$ data that is between 3 and 2 digits accurate and recovery 1 to 2 digits of accuracy in the conductance at varying levels of noise.

Recovery of the voltage from $I_{i,Ca,L}$ is a much more challenging problem in the presence of noisy data. The effect of noise is illustrated in 3.21. Even in the absence of noise, the objective function in both (3.63) and (3.66) does not have a unique minimizer. Furthermore, the noise introduces small perturbations in the recovery of the gating variable, m_L. As a result of the sensitivity of m_L to small perturbations

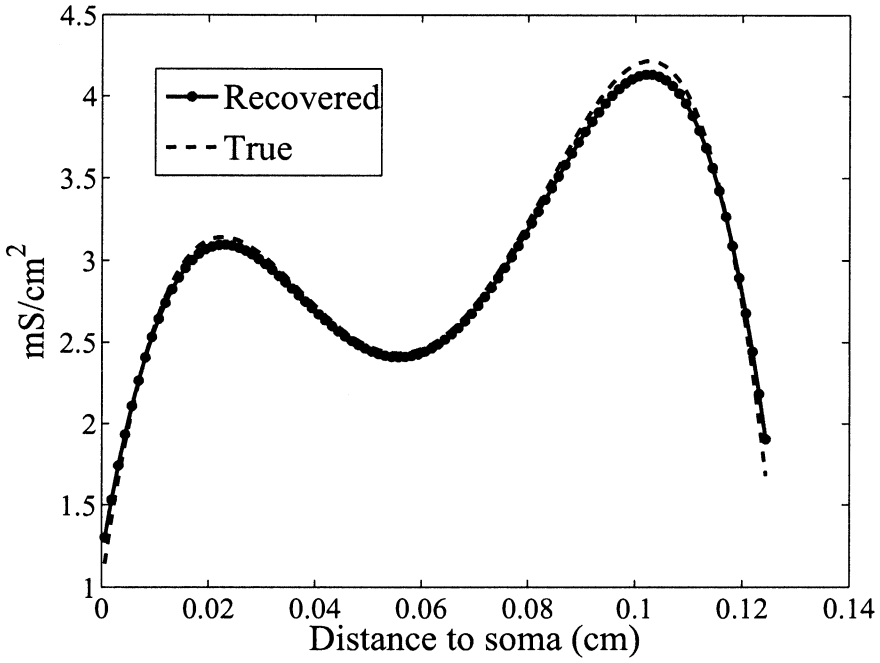

Figure 3.18: In the figure, we have recovered $g_{i,Ca,L}$ at several different points on the fiber by averaging the conductance found through (3.58) and (3.61). We then recovered the conductance over the entire fiber by using a cubic spline interpolation.

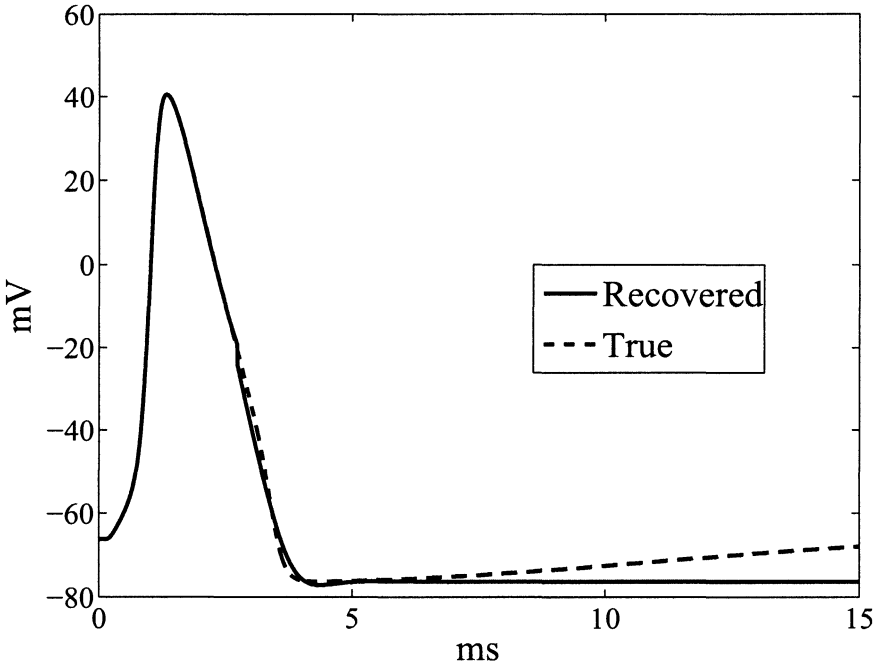

Figure 3.19: Illustration of the recovery of v from both $I^1_{i,Ca,L}$ and $I^2_{i,Ca,L}$. The "kink" in the recovered voltage is due to the fact that the objective function does not have a unique minimizer. The key to choosing the right one relies on uncertain transition voltage. Since this voltage is not known *a priori*, a best guess and bounding the solution is used.

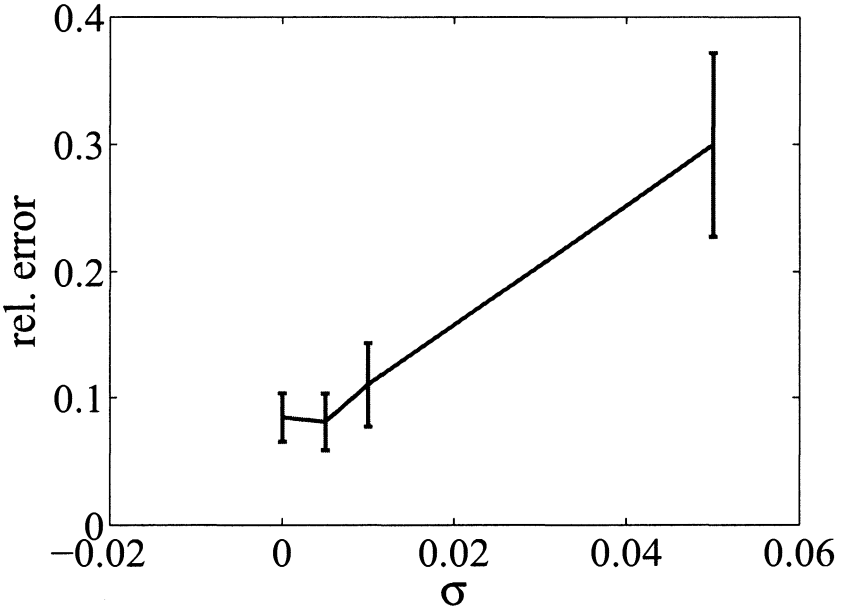

Figure 3.20: The mean and standard deviation of the relative error of the recovered conductance at recording sites are plotted for the varying levels of noise added to the calcium bound buffer. Buffer solutions were generated from random polynomials of degree ≤ 6 for $g_{i,Ca,L}$ before Gaussian noise with mean zero and standard deviation of $\sigma = [0\, 0.005\, 0.01\, 0.05]$ μM was added and averaged 200 times. Then I_{Ca} and g_{Ca} were recovered at each recording site.

as illustrated in figure 3.21(b), the recovery of the voltage is not robust. However, we still have partial information from the ratio of $I^1_{Ca,L}$ to $I^2_{Ca,L}$.

Recovery of g_{Ca} and v from these three channel types highlights their strengths and weaknesses. In general, we can see that the Morris-Lecar model is the most robust to noise in the data. This is due to the fact that it does not require as much information as the other channels. In the recovery of the currents due to the L–type channel and the H–type channel, we require knowledge of a time derivative of the current. For this reason, it might be best to engineer neurons to express the Morris-Lecar channel as a voltage sensor in the mammalian neurons instead of using *in vivo* calcium channels.

In the recovery of L–type channels, it might be possible to use multiple action potentials to change the intracellular calcium concentration. This would could provide the effect of a extracellular perturbation from which we could take the ratio of currents associated with the beginning and ends of an action potential trains. This would eliminated the need for two different extracellular calcium concentrations in our experimental setup.

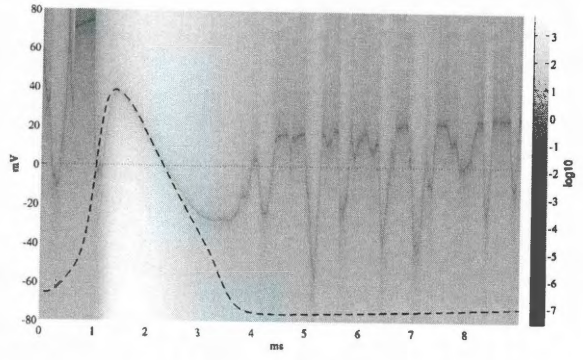

(a) Objective function for (3.63) and (3.66)

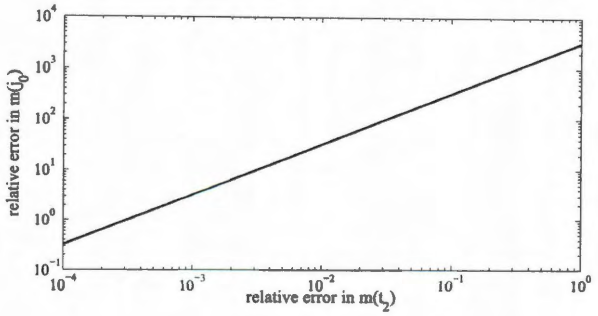

(b) Sensitivity of m_L to initial conditions

Figure 3.21: The objective function is shown for (3.63) and (3.66) from $I_{i,Ca,L}$ recovered from averaged calcium bound buffer with Gaussian noise mean zero and 0.05 μM standard deviation. The contour plot in 3.21(a) shows the value of the objective function at each point in time, t_j if both v and m_L had been computed exactly for $t < t_j$. In 3.21(b), we see the effect of perturbations in $m(t_2)$ on the relative error in $m(j_0)$. The true voltage (dotted) is superimposed on the contour plot.

3.8 Recovery of the potassium conductance

The recovery of $v_i(t)$ at each recording site required no additional information about the active properties of the neuron. In the experiment to recover the calcium current and the calcium channel densities, we were able to recover spatially distributed voltage data. Since calcium actually contributes relatively little to the voltage dynamics, the recovered voltage data should contain additional information about other unknown channel densities. Many experimentalists believe the sodium channel density to be relatively constant through the dendritic arbor. In certain neurons, changes in the potassium channel density play an important role in synaptic integration. The relationship between the spatially varying potassium conductance, g_K, and voltage is given by the Hodgkin-Huxley equation that relates the response of voltage to a current injection

$$\begin{aligned} C_m \partial_t v &= G_i \partial_{xx} v - g_L(v - E_L) - n^4 g_K(x)(v - E_K) - g_{Na} m^3 h (v - E_{Na}) \\ &\quad - I_{Ca}(x,t) - I(t)\delta(x - x_0) \\ \partial_t n = \frac{n_\infty(v) - n}{\tau_n}, &\quad \partial_t m = \frac{m_\infty(v) - m}{\tau_m}, \quad \partial_t h = \frac{h_\infty(v) - h}{\tau_h} \end{aligned} \tag{3.67}$$

where v satisfies the no flux boundary conditions

$$\partial_x v(0,t) = \partial_x v(l,t) = 0 \tag{3.68}$$

for a length l (cm) fiber with radius a (cm). E_L, E_K and E_{Na} (mV) are the transmembrane driving potentials determined by Nernst's equation. g_K, g_L and g_{Na} are the conductance densities (mS/cm^2) associated with their respective channels. C_m (mF/cm^2) is the membrane capacitance density. G_i (mS) is the axial conductivity computed from the axial resistance by $G_i = a/(2R_i)$. $I_{Ca}(x,t)$ (μA/cm^2) is the current density associated with voltage–sensitive calcium channels. In the experimental setting, we often denote by $I(t)$ (μA/cm^2) the injected current density on the neuronal fiber at the point x_0. Finally, when we consider the fiber in the rest state, then

$v(x,0) \equiv v_0(x)$ satisfies the following

$$\begin{aligned} G_i v_0'' = g_L(v_0 - E_L) + g_K(x) n_\infty (v_0^4 (v_0 - E_K) \\ + g_{Na} m_\infty (v_0^3 h(v_0(x))(v_0 - E_{Na}) + I_{Ca}(x,0)\,. \end{aligned} \tag{3.69}$$

We have deliberately written $g_K(x)$ as a function of x to emphasize its spatial dependence. Experimentally, almost all the quantities in (3.67) are known except for $I_{Ca}(x,t)$ which we have already recovered, and $g_K(x)$. We ask then if knowledge of spatially distributed time course voltage data, $\{v_i(t)\}_{i=1}^B$, can determine the potassium conductance, $g_K(x)$. We shall follow two lines of attach to this problem. The first approach mirrors our recovery of calcium information by ignoring the spatial dependence of g_K on the data and trying to recover the local potassium conductance where

$$g_{i,K} \equiv g_K(x_i) \tag{3.70}$$

from each individual voltage trace, $v_i(t)$. We then reconstruct the g_K by interpolation. The second approach is to use a least-squares optimization scheme to fit the correct value of $g_K(x)$.

3.8.1 Balancing charges to find g_K

There are several important observations that can be gleamed by considering the different currents at work in a patch of neural membrane. In the derivation of the Hodgkin-Huxley equations, we relied on balancing all the currents in a patch of neuron.

If we consider the total number of ions, or charge, then we can see that the neuron must maintain charge balance in a patch of neuron that starts at rest and returns to rest after a perturbation. Charges can flow through membrane channels as well as into and out of the neuronal patch. However, the charge flowing through the channels largely determines the total amount of charge entering and leaving the patch. In a simplified neuron with only sodium and potassium channels, sodium channels allow

sodium ions to move out of the cell. In order to bring the patch back to rest, potassium channel must open and balance the net charge that has left the cell. There is a small amount of charge that can be lost from axial currents. Therefore, the total charge is determined by the charges flowing through the membrane. As a result, we can scale one of the membrane currents to balance the charges implied by all of the other currents.

We define the total energy in any given patch of neuron by

$$V_0(x) = \int_0^T v(x,t)\,dt\,. \tag{3.71}$$

Since we assume that our patch starts and ends at rest, we know

$$v(x,0) = v(x,T) \tag{3.72}$$

but not necessarily the resting value. We can then see that energy, $V_0(x)$, satisfies the following differential equation,

$$\begin{aligned} \int_{-\infty}^{\infty} G_i \partial_{xx} v\,dt &= \int_{-\infty}^{\infty} C_m \partial_t v\,dt + \int_{-\infty}^{\infty} \sum_{c=1}^{C} g_c(v-E_c) \prod_{f=1}^{F_c} w_{cf}^{q_{cf}}\,dt \\ G_i V_0''(x) &= \int_{-\infty}^{\infty} \sum_{c=1}^{C} g_c(v-E_c) \prod_{f=1}^{F_c} w_{cf}^{q_{cf}}\,dt \end{aligned} \tag{3.73}$$

with the boundary condition

$$V_0'(0) = V_0'(l) = 0\,. \tag{3.74}$$

We can consider two cases in understanding $V_0''(x)$. If the action potential wave form does not change over the domain, then the total energy will be constant and $V_0''(x) = 0$. On a finite length of fiber, this is not true. However, the total charge flowing axially into and out of the patch is very small compared to the total charge moved by membrane channels. We then approximate $V_0''(x) \approx 0$ and get the following

$$\int_{-\infty}^{\infty} \sum_{c=1}^{C} g_c(v-E_c) \prod_{f=1}^{F_c} w_{cf}^{q_{cf}}\,dt = 0\,. \tag{3.75}$$

This essentially says that the sum of all the charges associated with each channel must equal each other. For the Hodgkin-Huxley equations, (3.67), (3.73) implies that at the recording site, x_i,

$$g_{i,K} = \frac{\int_0^T (g_{Na} m^3 h(v_i - E_{Na}) + I_{Ca,i,X}(t)\, dt}{\int_0^T n^4 (v_i - E_K)\, dt}. \tag{3.76}$$

Returning back to our problem, we have knowledge of all the objects on the right-hand side of (3.76) from either experimentally known functions and parameters or through our previous inverse problems. The gating variables, $\{n, m, h\}$ can be solved from the recovered voltage. By using (3.76), we are finding a constant $g_{i,K}$ that will locally balance the charges at a recording site. By applying (3.76) at each recording site and interpolating across the entire neuron, we can approximate the spatially varying potassium conductance. Figure 3.22 illustrates the recovery of a cubically varying potassium conductance by piecewise constant interpolation. Noise analysis was conducted by applying the charge balance equation, (3.73), to a large number of random polynomials of g_K for different levels noise in the bound buffer concentrations and recovery of the voltage and calcium current from our previous inverse problem. The relative error was calculated by comparing the recovered potassium conductances at the recording sites only. We see that noise can very quickly degrade the recovery of g_K through this method. This mainly reflects the sensitivity of accurately computing the gating variables, $\{n, m, h\}$, from noisy voltage data.

3.8.2 Recovery of g_K through least-squares

We consider now a second approach to recovering the potassium conductance. In this approach, we use a least-squares formulation to solve for g_K that will minimize the misfit between the data from our recording sites and a model dependent on g_K. In order to ease notation, we switch from the Hodgkin-Huxley equations to compact notion from (2.4) and (2.5) to describe voltage. We follow the approach taken by Cox [13] and articulate the problem of finding the spatially varying potassium

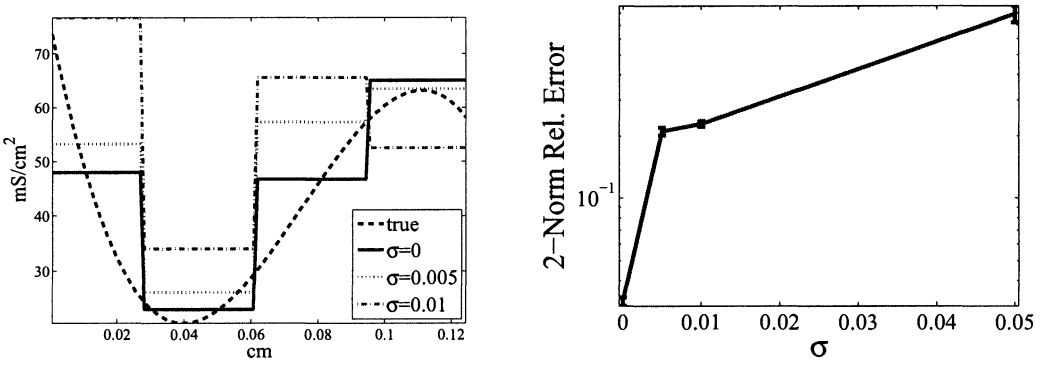

(a) Example recovery of g_K from charge balance (b) Error analysis for charge balance

Figure 3.22: An example of the use of the charge balance approximation to recover g_K is shown in 3.22(a). In this simulation, three different noise characteristics was added to calcium bound buffer before the voltage was recovered and used to recover g_K. Figure 3.22(b) shows the accuracy of charge balance in recovering g_K. Random polynomial of degree ≤ 6 were used to generate data. Again, noise was added to the calcium bound buffer before recovery of the voltage.

conductance through a least-squares formulation where we seek the solution to the following problem

$$\min_{g_K} \quad \sum_i \int_0^T |v(x_i,t;g_K) - v^\sharp(x_i,t)|^2\,dt \quad (= \Phi(g_k)) \tag{3.77}$$

$$s.t. \quad C_m\partial_t v - G_i\partial_{xx}v + \sum_{c=1}^{C} g_c(x)(v-E_c)\prod_{f=1}^{F_c} w_{cf}^{q_{cf}} + I(t)\delta(x-x_0) = 0 \tag{3.78}$$

$$\partial_t w_{cf} - \frac{w_{cf,\infty}(v) - w_{cf}}{\tau_{cf}(v)} = 0 \tag{3.79}$$

$$G_i v_0'' - \sum_{c=1}^{C} g_c(x)(v_0 - E_c)\prod_{f=1}^{F_c} w_{cf,\infty}^{q_{cf}}(v_0) = 0\,. \tag{3.80}$$

At this point, the discretized version of (3.77) with a descent algorithm that estimates the gradient of Φ through finite differencing can be used to get an approximate solution. The discretized potassium conductance will turn (3.77) into a problem in $\mathbb{R}^n$. Using a line search method to solve (3.77) will require $n+1$ solutions to (2.4) [54]. The discretized version of a realistic neuron can lead to 500 equations to approx-

imate (2.4) on the neuronal geometry. For n large, this problem is computationally prohibitive from being carried out by experimentalists. When using the least-squares framework, they will often make underlying assumptions on parameters of interest to reduce the number of free variables. For example, one can assume that g_K increases linearly away from the soma to reduce the parameter search to two variables. This may be true for a few neuron types, but is not true in general. Furthermore, it would be difficult to obtain this kind of information for all neurons.

To move away from any assumptions on g_K, we shall calculate the gradient of (3.77) thereby making computations faster and more reliable by only assuming that g_K is piecewise constant over the neuronal geometry. We first form the associated **Lagrangian**, $\mathcal{L}$, to (3.77) which liberates v in the sense that it only satisfies the boundary conditions $\partial_x v(0,t) = \partial_x v(l,t) = 0$. The Lagrangian associated with (3.77) is

$$\mathcal{L}(g_K, v, V, w_{cf}, W_{cf}, v_0, V_0) = \sum_i \int_0^T |v(x_i,t;g_K) - v^\sharp(x_i,t)|^2\,dt \tag{3.81}$$

$$+ \int_0^T \int_0^l \left(C_m \partial_t v - G_i \partial_{xx} v + \sum_{c=1}^{C} g_c(x)(v - E_c) \prod_{f=1}^{F_c} w_{cf}^{q_{cf}} + I(t)\delta(x - x_0) \right) V\,dxdt$$

$$+ \int_0^T \int_0^l \left(\partial_t w_{cf} - \frac{w_{cf,\infty}(v) - w_{cf}}{\tau_{cf}(v)} \right) W_{cf}\,dxdt \tag{3.82}$$

$$+ \int_0^l \left(G_i v_0'' - \sum_{c=1}^{C} g_c(x)(v_0 - E_c) \prod_{f=1}^{F_c} w_{cf,\infty}^{q_{cf}}(v_0) \right) V_0\,dx\,. \tag{3.83}$$

Solutions to (3.77) can be found at the following critical points of the Lagrangian [44] and [19],

$$\partial_{v,v_0,w_{cf}} \mathcal{L} = \partial_{V,V_0,W_{cf}} \mathcal{L} = 0\,.$$

First we note that $\partial_{v,v_0,w_{cf}} \mathcal{L} = 0$ is a restatement of (2.4) and (2.5) and referred to as the state equations. In order to solve $\partial_{V,V_0,W_{cf}} \mathcal{L} = 0$, we differentiate $\mathcal{L}$ at $\{\bar{v}, \bar{w}_{cf}, \bar{v_0}\}$ in the direction of $\{\tilde{v}, \tilde{w}_{cf}, \tilde{v_0}\}$ where $\partial_x \tilde{v}(0,t) = \partial_x \tilde{v}(l,t) = 0$ and integrate by parts to

get the following adjoint equations corresponding to our three generalized constraints

$$-C_m\partial_t V - G_i\partial_{xx}V + \sum_{c=1}^{C} g_c V \prod_{f=1}^{F_c} w_{cf}^{q_{cf}} - \partial_v Q_{cf}(\bar{v},\bar{w}_{cf})W_{cf} \qquad (3.84)$$
$$+ \sum_i \delta(x-x_i)(v(x_i,t;g_K) - v^\sharp(x_i,t)) = 0$$

where $V(x,T) = 0$ and $\partial_x V(0,t) = \partial_x V(l,t) = 0$,

$$-\partial_t W_{cf} - \partial_{w_{cf}} Q(\bar{v},\bar{w}_{cf})W_{cf} + \sum_{c=1}^{C} g_c(v-E_c)\prod_{f=1}^{F_c} q_{cf}\bar{w}_{cf}^{q_{cf}-1}V = 0 \qquad (3.85)$$

where $W_{cf}(x,T) = 0$ and

$$G_i V_0'' - \sum_{c=1}^{C}\left(g_c\prod_{f=1}^{F_c} w_{cf,\infty}^{q_{cf}}(\bar{v_0}) + g_c(\bar{v_0}-E_c)\prod_{f=1}^{F_c} q_{cf}w_{cf,\infty}^{q_{cf}-1}(\bar{v_0})\right)V_0 \qquad (3.86)$$
$$-C_m V(x,0) - W_{cf}(x,0) = 0$$

where $V_0'(0) = V_0'(l) = 0$. Therefore, for a given candidate, $g_{\bar{K}}$, we have solutions to (2.4),(2.5), (3.84), (3.85) and (3.86). We then say that the gradient of $\mathcal{L}$ at $g_{\bar{K}}$ in the direction of $g_{\tilde{K}}$ is

$$\langle \nabla\mathcal{L}(v,V,v_0,V_0,w_{cf},W_{cf}), g_{\tilde{K}}\rangle = \int_0^T\int_0^l w_{21}^4(v-E_2)Vg_{\tilde{K}}\,dx\,dt \qquad (3.87)$$
$$+ \int_0^l w_{21,\infty}(v_0)^4(v_0-E_2)V_0 g_{\tilde{K}}\,dx$$
$$= \int_0^T\int_0^l n^4(v-E_K)V\,dx\,dt + \int_0^l n_\infty(v_0)(v_0-E_K)V_0\,dx\,.$$

The implementation to solutions of (2.4), (2.5), (3.84), (3.85) and (3.86) is described in appendix A.1. Specifically, we use a semi-implicit trapazoidal rule for the solution of the state equation (2.4) and (2.5) and backward Euler method for the solution to the adjoing equations (3.84) – (3.86). Since the different marching schemes are used for the state and ajoint equations, the computed discrete gradient, $\nabla\Phi(g_K)$, is not gradient of the discretized objective function $\Phi_h(g_K)$. We examine the error in our computed gradient approximation next.

In figure 3.23, we checked to see that the objective function, Φ, and its gradient, $\nabla\Phi$, converged to zero in a local neighborhood around the solution to (3.77). We sampled the objective function on the ball of radius σ from the solution and calculated

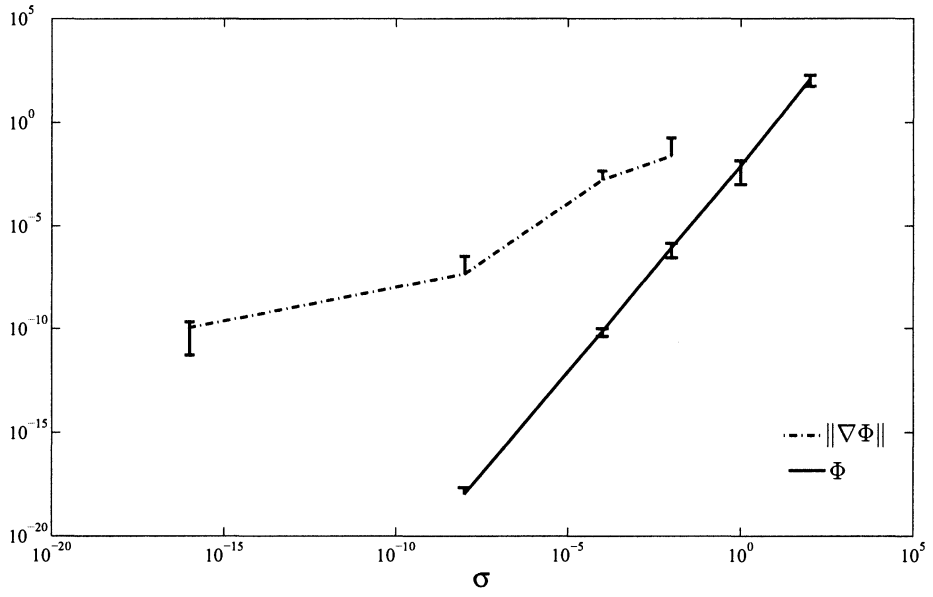

Figure 3.23: 10 random conductance distributions, g_K, were taken from the true solution, g_{K0}, such that $\|g_K - g_{K0}\| = \sigma$. The resulting mean and standard deviation for the objection function and normed gradient are plotted above.

the values of Φ and $\|\nabla\Phi\|$. The average values and the standard deviations are plotted. We see convergence to 0 for both Φ and $\nabla\Phi$ as $\sigma \to 0$.

We also compared our gradient calculation to those obtained via finite differencing in figure 3.25. The gradients from finite differencing and adjoints are shown component wise on a log plot in a small neighborhood of the solution. We can see that the two gradient approximations do not match each other. The adjoint based gradient does seem to maintain a fixed error as the two gradients approach the solution. We explore this idea through numerical experiments by testing whether there exists an $n \geq N$ where

$$\frac{\|\nabla_{ad}\Phi_n - \nabla_{fd}\Phi_n\|}{\|\nabla_{ad}\Phi_n\|} \leq 1 \quad \text{as} \quad g_K^n \to \bar{g}_K \tag{3.88}$$

where $\nabla_{ad}\Phi_n$ is the adjoint approximation to the finite difference gradient, $\nabla_{fd}\Phi_n$, at the current approximation, g_K^n, to the solution, $\bar{g}_K$. Through some numerical experimentation, we see that close enough to the solution, our adjoint gradient is accurate

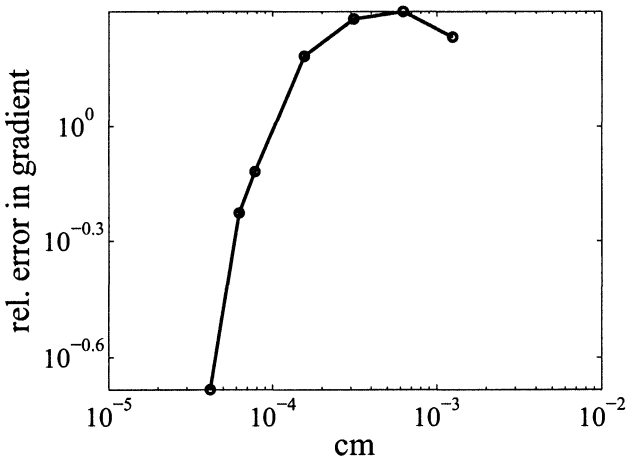

Figure 3.24: Starting from an iterate where the adjoint was unable to get one digit of accuracy, successive refinements of the spatial grid to solve both the state and adjoint equations was able to recover greater accuracy with the finite difference gradient. The diminishing accuracy with each refinement of the grid is a consequence that we are approaching the errors introduced by the time discretization.

enough to ensure convergence to the solution. Moreover, we explore the source of the error between the two gradients. Principally, the divergence between the two gradients is accounted in the numerical implementation of the adjoint equations. Since we can only approximate the adjoint equations, we are solving for approximations of the gradient. As both the spatial and temporal grids are refined, we expect our approximation to converge to the true solution of the adjoint equations. As a result, we should see that refinement in the grids also causes the adjoint gradient to approach the finite difference gradient. In figure 3.24, we start at an iterate so that the relative error between the two gradients is greater than one. we see that as the spatial grid is refined, $h \to 0$, implies that $\|\nabla_{ad}\Phi - \nabla_{fd}\Phi\| \leq 1$. However, to gain accuracy, we would have to dramatically decrease h and increase the size of the matrix representations of our adjoint and state equations. For realistic neuronal geometries, its is not feasible to solve the adjoint equations beyond one digit of accuracy before running into memory problems. Therefore, we use a trust-region method [7] with

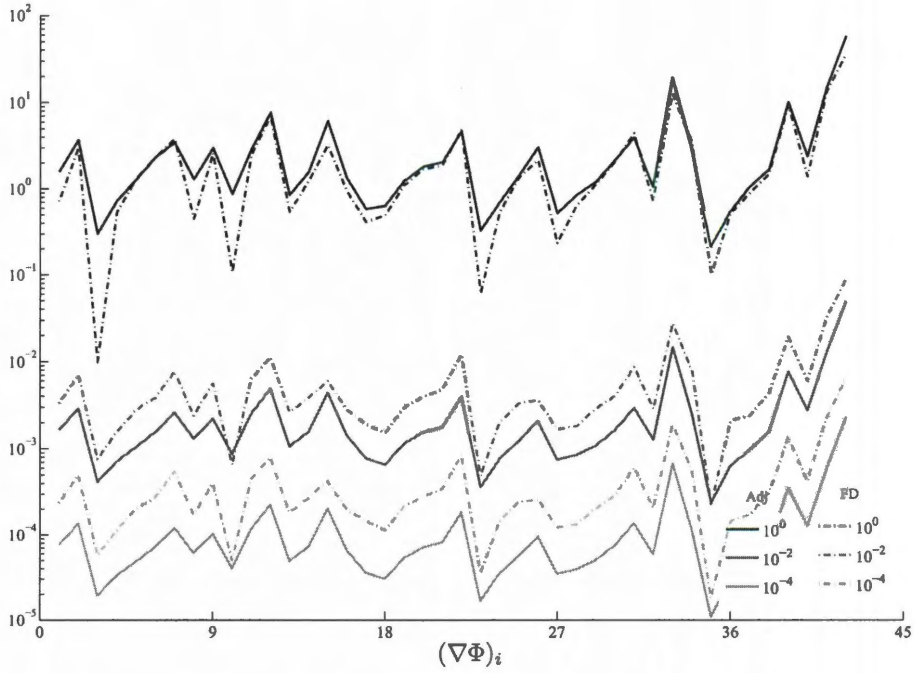

Figure 3.25: The figure shows the convergence of finite difference, *dotted*, and adjoint, *lined*, calculated gradients for three different successively smaller starting guess, g_K, where $g_K = g_{K0}.*(1+\mathcal{N}(0,\sigma)))$ and σ varies from $10^0 \rightarrow 10^{-4}$. Although the relative error between the two gradients does not converge, they both converge to zero as the starting guesses move closer to the true solution.

a gradient stopping criteria adjusted to the accuracy expected from the accuracy of the discretization. For iterates not close to the solution, we see in table 3.1 that the Hessian, $\nabla^2\mathcal{L}$, is not positive definite. This can be a problem for line search based decent algorithms. Our numerical experiments have shown that in the presence of noisy data, line search methods can find iterates far from previous iterates causing numerical problems in solving the state and adjoint equations.

In figure 3.26, we consider the solution to (3.77) on a fiber where we see $v^\sharp$ given in figure 3.26(a). In figure 3.26(b), we show the starting guess, approximate solution and actual value for g_K. The step-like nature of the approximate solutions occurs from the piece-wise constant assumptions on g_K.

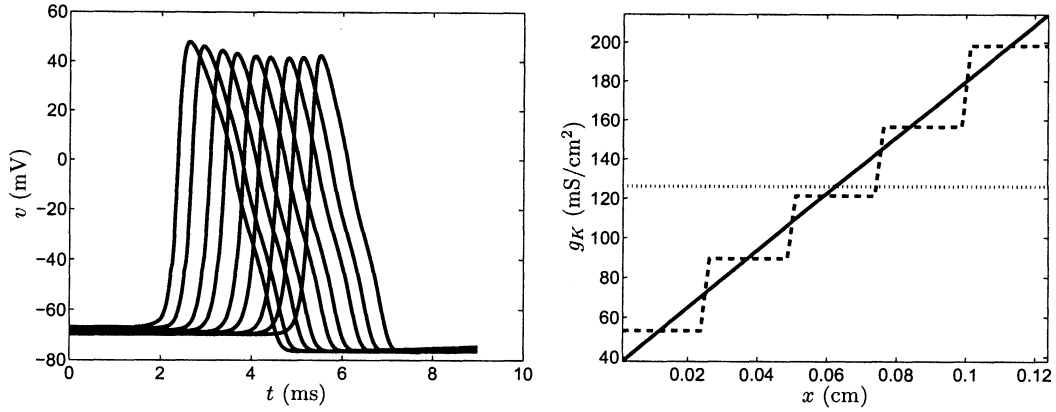

(a) (b)

Figure 3.26: Fig. 3.26(a) shows distributed time series voltage data used in the adjoint equations. Fig. 3.26(b) show the initial guess (..), the true solution (–) and the recovered g_K (- -) after convergence.

Finally, we consider the recovery of g_K from partial voltage information at each of our recording sites. In the recovery of the voltage from $I_{Ca,L}$, the recovered voltages are only available over an interval.

3.8.3 Preconditioning the least-squares problem

The least-squares approach to find g_K has several advantages over the charge balance approach. The resolution of recovery in g_K is limited by the number of recording sites. Because charge balance does not take into account the axial currents flowing in the dendritic tree, it can not be used to infer information about the locations between recording sites. It can not handle partial voltage information. Finally, numerical experiments have shown it to be sensitive to noise in the voltage data. Least-square methods do not suffer from any of these drawbacks. However, computationally, the least-squares approach is much more expensive to compute. Also, if the starting guess to g_K is poor, the algorithm can demonstrate poor convergence from inaccurate gradient calculations. We can combine both approaches to take advantage of each algorithm's strengths. Specifically, we can use charge balance as a quickly calcula-

ble initial guess for our least-squares algorithm. This should allow least-squares to converge quicker to the optimal solution by starting in a neighborhood where the adjoint gradient is much more accurate. Furthermore, we can recover g_K with a finer discretization than charge balance. In figure 3.27, the initial guess was provided by the charge balance equation. The adjoint methods then refined the recovered g_K. Numerical experiment have shown that using charge balance as a starting guess reduces the number of iteration till convergence by one half.

iter	rel. error	Φ	$\|\nabla\Phi\|_2$	$\lambda_{min} \in \rho(\nabla^2 F)$
1	5.80×10^{-1}	3.33×10^{4}	3.15×10^{2}	-1.200
2	4.83×10^{-1}	2.04×10^{4}	2.98×10^{2}	-0.803
3	4.00×10^{-1}	8.91×10^{3}	1.84×10^{2}	-0.685
4	2.96×10^{-1}	4.34×10^{3}	1.27×10^{2}	-0.478
5	2.06×10^{-1}	1.12×10^{3}	8.90×10^{1}	0.153
6	1.42×10^{-1}	3.48×10^{2}	3.33×10^{1}	0.241
7	7.03×10^{-2}	1.39×10^{2}	9.08×10^{0}	0.194
8	2.19×10^{-2}	1.06×10^{2}	3.25×10^{0}	0.140
9	2.44×10^{-2}	1.05×10^{2}	1.29×10^{0}	0.138
10	2.44×10^{-2}	1.05×10^{2}	1.29×10^{0}	0.138

Table 3.1: The relative error 2-norm error in the current iterate, the objective function value, Φ, the 2-norm of the gradient of the objective function, $\|\nabla\Phi\|_2$, and the smallest eigenvalue of the Hessian approximation to Φ, $\nabla^2\Phi$, is shown in the following table for each iteration in the optimization procedure to recover the potassium conductance on a fork.

3.8.4 Recovery of g_K on realistic geometries

Numerical experiments seems to indicate that convergence to the solution under more complex geometries is slower than simple geometries. This phenomenon is seen when the gradient is calculated via adjoints or finite difference. One possible explanation is

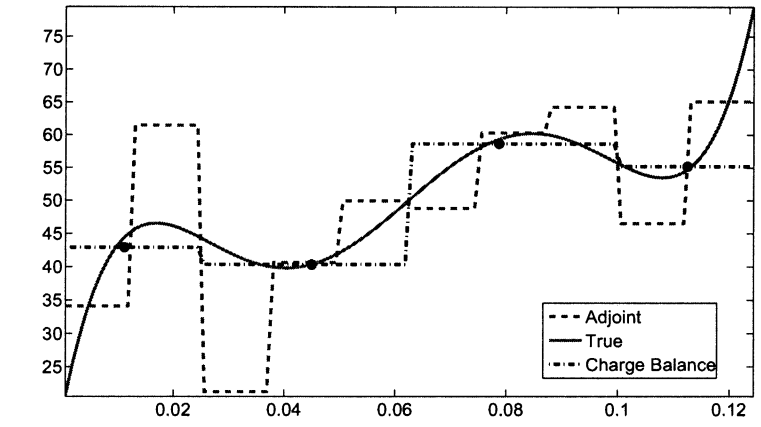

(a)

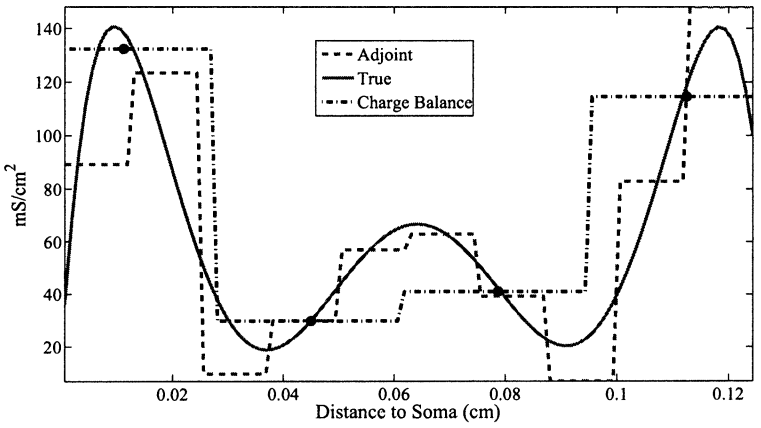

(b)

Figure 3.27: We see the recovery of g_K for two different functions over the fiber where the initial guess has been given by charge balance. The g_K grid for the adjoint equations is chosen to be half the size of the recording sites. We can see in the recovery on top that adjoints does run into issues. However, in general, it an provide a finer discretization of g_K.

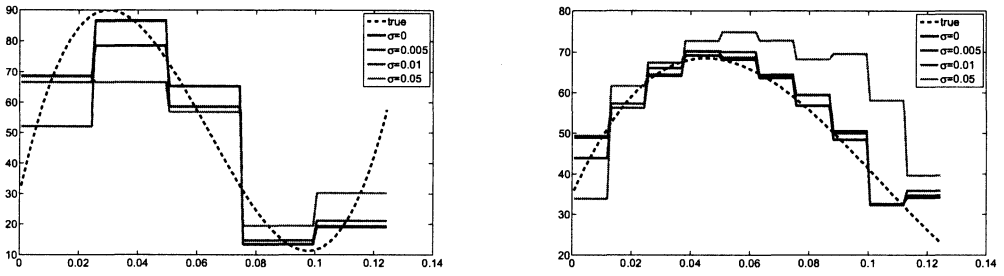

(a) cubic (b) quintic

Figure 3.28: Recovery of g_K for a cubic 3.28(a) and quintic 3.28(b) polynomial for three different noise profiles in the calcium bound buffer. As the standard deviation increases, we generally see small degradation in the recovered value. An exception is the quintic polynomial for the $\sigma = 0.05$ where regularization of the calcium current at one recording site is not able to smooth away enough noise.

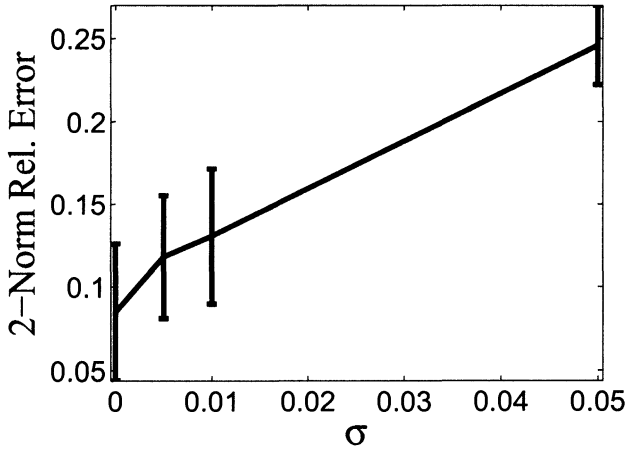

Figure 3.29: The relative error in the recovery of g_K of random polynomials of degree ≤ 6 from noisy data. First, 10 random polynomials whose range was bounded between 20 and 150 mS/cm^2 were used to generate calcium bound buffer data, b. Then Gaussian noise with mean zero and standard deviation, [00.0050.010.05], was added and averaged 200 times. Then the passive calcium parameters were recovered, and the voltage and calcium current from the Morris-Lecar calcium channel model. The voltage data was used as $v^\sharp$ in the adjoint code. The mean and standard deviation of the relative error of the recovered potassium conductance at the recording sites is shown in the graph above.

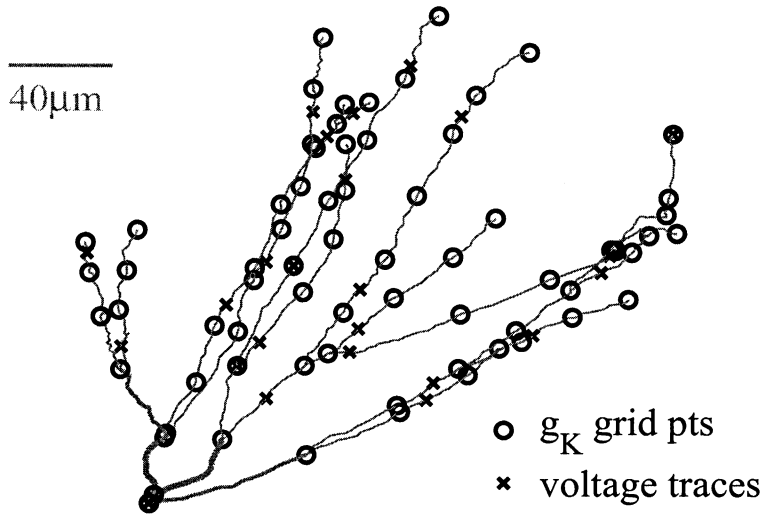

Figure 3.30: The recording locations and the g_K grid points are shown on the biophysically accurate neuronal geometry.

that branches in larger trees are isolated from one another. Changes in the potassium conductance in part of the tree do not effect the rest of the tree. Therefore, the optimization algorithm can slow as it tries to optimize in certain location on the tree. Moreover, on the fiber, the optimization routine always fits the potassium conductance closest to the current injection point before moving farther away. On more complex geometries, the optimization routines seems to slowly fit the most distal branches before getting near the trunk of the tree where the current is injected. Since action potentials propagate from the trunk out to the distal branches, it will be hard for the decent algorithm to find the potassium conductance farther away without knowing the axial currents that shaped the action potential's arrival.

In the following simulation in figure 3.8.4, we calculated the voltage changes associated with a step current injection near the soma.

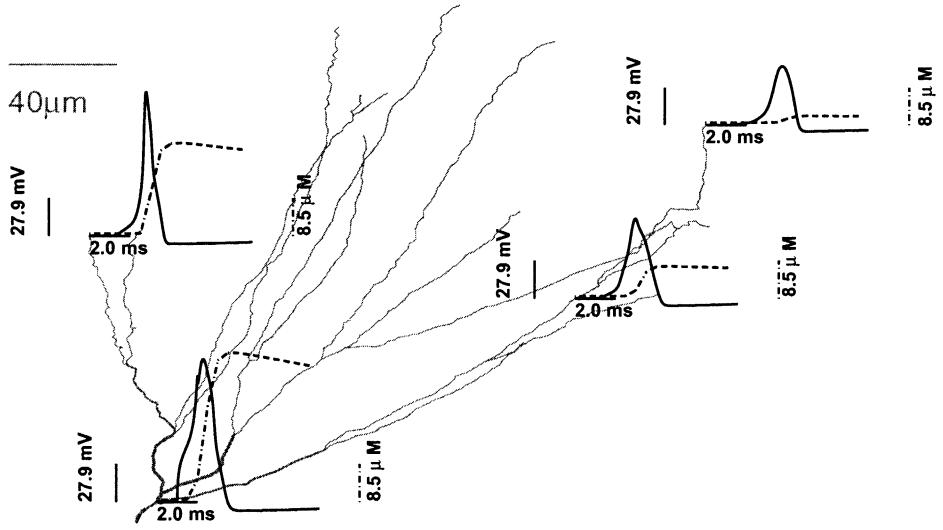

Figure 3.31: The voltage traces are shown for a few different locations on the neuronal geometry. In this simulation, the potassium conductance increases with distance from the soma. As a result, the action potentials are distinctly attenuated away from the soma.

Appendix A

Appendix

A.1 Numerical solution to the Hodgkin-Huxley, calcium and adjoint equations

We solve the Hodgkin-Huxley, 2.1 and 2.3, and the adjoint equations, 3.84, 3.85 and 3.86, with an approximate trapezoid rule in time and finite elements in space. We partition space and time into the following grids

$$[0, h, 2h, ..., (N_x - 1)h = l] \text{ and } [0, \tau, 2\tau, ..., (N_t - 1)\tau = T] \tag{A.1}$$

and approximate our state and adjoint variables as piecewise linear and conductances as piecewise constant. More precisely

$$\begin{aligned} f(x, (j-1)\tau) &= \sum_{i=1}^{N_x} \mathbf{f}_{i,j} H_i(x) \quad f = \{\mathbf{v}, \mathbf{V}, \mathbf{w}_{cf}, \mathbf{W}_{cf}\} \\ y(x) &= \sum_{i=1}^{N_x} \mathbf{y}_i H_i(x) \quad y = \{\mathbf{v}_0, \mathbf{V}_0\} \\ g_c(x) &= \sum_{i=1}^{N_x - 1} \mathbf{g}_{c_i} \chi(x), \quad c = \{Ca,\ K,\ L,\ Na\} \end{aligned} \tag{A.2}$$

where

$$H_i(x) = \begin{cases} 1 - |x - (i-1)h|/h & \text{if } (i-2)h < x < ih \\ 0 & \text{otherwise} \end{cases}$$

$$\chi_i(x) = \begin{cases} 1 & \text{if } (i-2)h < x < ih \\ 0 & \text{otherwise} \end{cases}$$

After substitution of these representations into the weak form, we get the following equations. We define the following associated matrices

$$\mathbf{M}(i,i+1) = \frac{h}{6} \quad \mathbf{M}(i,i) = \frac{h}{6} \begin{cases} 2 & \text{if } i = 1, N_x \\ 4 & \text{otherwise} \end{cases}$$

$$\mathbf{K}(i,i+1) = -\frac{1}{h} \quad \mathbf{K}(i,i) = \frac{1}{h} \begin{cases} 1 & \text{if } i = 1, N_x \\ 2 & \text{otherwise} \end{cases}$$

$$\mathbf{L}(i,i+1) = \mathbf{GL}_i \frac{h}{6} \quad \mathbf{L}(i,i) = \frac{h}{6} \begin{cases} 2\mathbf{GL}_1 & \text{if } i = 1 \\ 2\mathbf{GL}_{N_x} & \text{if } i = N_x \\ 2(\mathbf{GL}_{i-1} + \mathbf{GL}_i) & \text{otherwise} \end{cases}$$

and function

$$\mathbf{N}(\mathbf{GC}, \mathbf{v}, \mathbf{w})_i = \frac{h}{12} \Big(\sum_{j=i-1}^{i} \mathbf{GC}_j (\mathbf{v}_j + \mathbf{v}_{j+1})(\mathbf{w}_j + \mathbf{w}_{j+1}) + 4\mathbf{v}_i \mathbf{w}_i \Big) .$$

which is used to evaluate all of the nonlinear forms that arise in the weak from by approximation as a bilinear form. From 2.5 we get the following nonlinear equation

$$(G_i\mathbf{K} - \mathbf{L})\mathbf{v}_0 - \sum_{c=1}^{C} \mathbf{N}(\mathbf{GC}, (\mathbf{v}_0 - E_c), \prod_{f=1}^{F_c} w_{cf,\infty}^{q_{cf}}(\mathbf{v}_0)) = 0 \tag{A.3}$$

which is solved for $\mathbf{v}_0$. We find $\mathbf{v}_0$ using a call to `fsolve` in `MATLAB` which uses a user-supplied Jacobian of (A.3) in an Newton based descent scheme. The Jacobian of (A.3) is given by

$$\begin{aligned} \mathbf{J} = (G_i\mathbf{K} - \mathbf{L}) - \sum_{c=1}^{C} \Bigg(& \mathbf{N}(\mathbf{GC}, \prod_{f=1}^{F_c} w_{cf,\infty}^{q_{cf}}(\mathbf{v}_0)) \\ & + \mathbf{N}(\mathbf{GC}, \mathbf{v}_0 - E_c)\, \mathtt{diag} \left(\prod_{f=1}^{F_c} q_{cf} w_{cf,\infty}^{q_{cf}-1}(\mathbf{v}_0) \right) \Bigg) . \end{aligned} \tag{A.4}$$

The solution, $\mathbf{v}_0$, is the starting value used in the recursion that results from the time dependent problem 2.4. This system of odes are solved with a linearized trapezoid scheme

$$C_m\mathbf{M}\mathbf{v}_j - C_m\mathbf{M}\mathbf{v}_{j-1} = \tau/2\left[(G_i\mathbf{K}+\mathbf{L})\mathbf{v}_j - \sum_{c=1}^{C}\mathbf{N}\left(\mathbf{GC}, \mathbf{v}_j - E_c, \prod_{f=1}^{F_c}\mathbf{w}_{cf_j}^{q_{cf}}\right) - \mathbf{S}_j\right] \tag{A.5}$$

$$+\tau/2\left[(G_i\mathbf{K}+\mathbf{L})\mathbf{v}_{j-1} - \sum_{c=1}^{C}\mathbf{N}\left(\mathbf{GC}, \mathbf{v}_{j-1} - E_c, \prod_{f=1}^{F_c}\mathbf{w}_{cf_{j-1}}^{q_{cf}}\right) - \mathbf{S}_{j-1}\right] \tag{A.6}$$

where we solve for $\mathbf{v}_j$ by assuming

$$\mathbf{N}\left(\mathbf{GC}_j, \mathbf{v}_j - E_C, \prod_{f=1}^{F_c}\mathbf{w}_{cf_j}^{q_{cf}}\right) \approx \mathbf{N}\left(\mathbf{GC}_{j-1}, \mathbf{v}_{j-1} - E_C, \prod_{f=1}^{F_c}\mathbf{w}_{cf_{j-1}}^{q_{cf}}\right) \tag{A.7}$$

to get the following

$$((2/\tau)C_m\mathbf{M} - G_i\mathbf{K} - \mathbf{L})\mathbf{v}_j = ((2/\tau)\mathbf{M} + G_i\mathbf{K} + \mathbf{L})\mathbf{v}_{j-1} \tag{A.8}$$

$$-2\mathbf{N}\left(\mathbf{GC}_{j-1}, \mathbf{v}_{j-1} - E_C, \textstyle\prod_{f=1}^{F_c}\mathbf{w}_{cf_{j-1}}^{q_{cf}}\right) - (S_j + S_{j-1}) \tag{A.9}$$

and similarly for 2.4 we get

$$(2/\tau)\mathbf{M}\mathbf{w}_{cf_j} = (2/\tau)\mathbf{M}\mathbf{w}_{cf_{j-1}} + 2\mathbf{M}\frac{\mathbf{w}_{cf,\infty}(\mathbf{v}_{j-1}) - \mathbf{w}_{cf_{j-1}}}{\tau_{cf}(\mathbf{v}_{j-1})} \tag{A.10}$$

In figure A.1, we show the solution to (2.1) on a fiber. We can see how the calcium and calcium bound buffer mimic the traveling action potential in the voltage equations.

The adjoint equations in 3.84, 3.85 and 3.86 are treated differently than the forward equations, 2.4. These equations are linear in the unknown adjoint variable. Therefore, we compute these equations by using a similar spatial discretization scheme but use backward Euler in time. Unlike the forward equations, we are solving the adjoint equations backward in times given a final condition. For 3.84 we get

$$-C_m\mathbf{M}\mathbf{V}_{j+1} + C_m\mathbf{M}\mathbf{V}_j = G_i\mathbf{K}\mathbf{V}_j + \left(\textstyle\sum_{c=1}^{C}\mathbf{N}(g_c, \prod_{f=1}^{F_c}\mathbf{w}_{cf}^{q_{cf}})\right)\mathbf{V}_j$$
$$-\left(\textstyle\sum_{c=1}^{C}\mathbf{N}(1, \partial_w Q_{cf}(\bar{v}, \bar{w}_{cf}))\right)\mathbf{W}_{cf_j} + \mathbf{E}_j$$

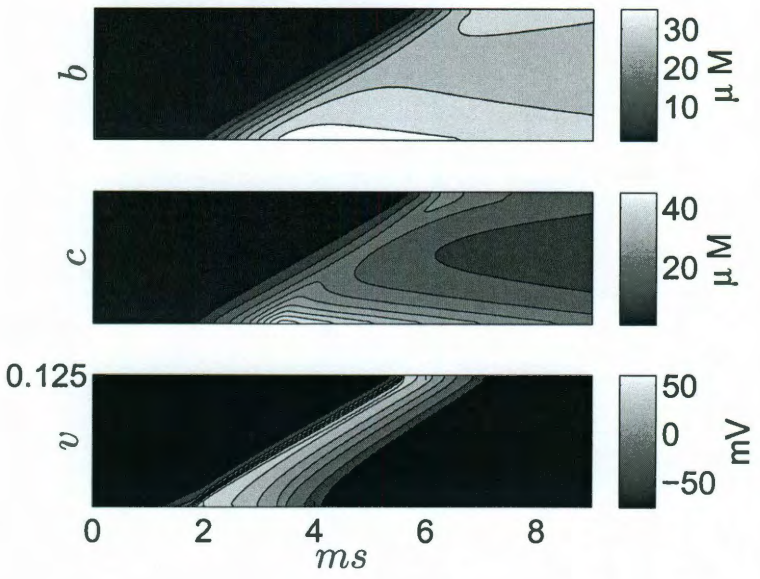

Figure A.1: The numerical solution to the calcium–buffer-voltage system, (2.12) and (2.1), is shown in three contour plots. For each panel, the x-axis is the length of the fiber and they y-axis is time. Starting from the top panel going down, the solution to the calcium bound buffer, then calcium and finally voltage is shown. We can see how both calcium and to a lesser extent, the bound buffer, mimics the traveling voltage wave.

and for 3.85 we get

$$-\mathbf{M}\mathbf{W}_{cf_{j+1}} + \mathbf{M}\mathbf{W}_{cf_j} = \mathbf{N}(1, \partial_{w_{cf}} Q(\bar{v}, \bar{w}_{cf}))\mathbf{W}_{cf_j} - \left(\sum_{c=1}^{C} \mathbf{N}(g_c, (\mathbf{v} - E_c) \prod_{f=1}^{F_c} q_{cf} \mathbf{w}_{cf}^{q_{cf}-1})\right) \mathbf{V}_j$$

which we can rewrite for $\mathbf{V}_j$ and $\mathbf{W}_{cf_j}$ and solve by recursion using the final condition that $\mathbf{V}_{N_t} = 0$ and $\mathbf{W}_{cf_{N_t}} = 0$. We then use $\mathbf{V}_1$ and $\mathbf{W}_{cf_1}$ to solve 3.86 and get the last adjoint variable by the following linear solve

$$G_i \mathbf{K}\mathbf{V}_0 - \left(\sum_{c=1}^{C} \mathbf{N}(g_c, \prod_{f=1}^{F_c} w_{cf,\infty}^{q_{cf}}(\mathbf{v}_0)) + \mathbf{N}(g_c, (\mathbf{v}_0 - E_c) \prod_{f=1}^{F_c} q_{cf} w_{cf,\infty}^{q_{cf}-1}(\mathbf{v}_0)\right) \mathbf{V}_0 - C_m \mathbf{V}_1 - \mathbf{W}_{cf_1} = 0\,.$$

In extending the numerical scheme to branched neurons, we enforce the branching conditions 2.7 by the introduction of a branched node whose support lies on all three branches that meet at the branch point. By convention, we label the last node on the parent as the branch node. Therefore for the kth branch point has a parent, p_k, and two children, c_k^1 and c_k^2. For simplicity, we consider branches with the same number of compartments, N_x. Then we define the the branch node as

$$H_{p_k,N_x}(x) = \begin{cases} H_{N_x}(x) & \text{if } x \text{ lies on } p_k \\ H_1(x) & \text{if } x \text{ lies on } c_k^1 \text{ or } c_k^2 \end{cases},. \tag{A.11}$$

For g_k, in defining the piecewise constant functions, χ, we restrict the support of χ onto a single branch. This results in the formulation of our forward and adjoint variables as follows on a branch, b,

$$f_b^{(j)}(x, (j-1)\tau) = \sum_{i=1}^{N_x} \mathbf{f}_{b,i}^{(j)} H_{b,i}(x) \quad f = \{\mathbf{v}, \mathbf{V}, \mathbf{w}_{cf}, \mathbf{W}_{cf}\} \tag{A.12}$$

$$y_b(x) = \sum_{i=1}^{N_x} \mathbf{y}_{b,i} H_{b,i}(x) \quad \mathbf{y} = \{\mathbf{v}_0, \mathbf{V}_0\} \tag{A.13}$$

$$g_{Kb}(x) = \sum_{i=1}^{N_x - 1} \mathbf{G}\mathbf{K}_{b,i} \chi_{b,i}(x)\,. \tag{A.14}$$

With revised definitions in hand, the resulting matrices that arise from the weak form in finite elements is amended to reflect the branching pattern of the neurons.

However, once these adjustments are made, the discretized recursion formulas are the same.

With the associated finite element matrices defined for the branched neuron, we can solve our calcium system. The resulting odes after FEM yields

$$\begin{aligned}
\mathbf{Mb}' &= D_b\mathbf{Kb} + k_p\mathcal{B}\mathbf{Mc} - k_m\mathbf{Mb} - k_p\mathbf{N}(\mathbf{c},\mathbf{b}) \\
\mathbf{Mc}' &= D_c\mathbf{Kc} - k_p\mathcal{B}\mathbf{Mc} + r\mathbf{Mc} + k_m\mathbf{Mb} + k_p\mathbf{N}(\mathbf{c},\mathbf{b}) - r\mathbf{M}c_0 \\
&\quad - \mathbf{N}(\mathbf{GCa}, m_\infty^{Ca}(\mathbf{v}), \mathbf{v} - E_{Ca})/(aF)
\end{aligned} \tag{A.15}$$

which results in the following recursion upon application of the linearized trapezoid rule,

$$\begin{aligned}
&((\tau/2)\mathbf{M} - D_b\mathbf{K} + k_m\mathbf{M})\mathbf{b}_{j+1} - k_p\mathcal{B}\mathbf{M}\mathbf{c}_{j+1} = ((\tau/2)\mathbf{M} + D_b\mathbf{K} - k_m\mathbf{M})\mathbf{b}_j \\
&\quad + k_p\mathcal{B}\mathbf{M}\mathbf{c}_j - 2k_p\mathbf{N}(\mathbf{c},\mathbf{b}) \\
&- k_m\mathbf{M}\mathbf{b}_{j+1} + ((\tau/2)\mathbf{M} - D_c\mathbf{K} + k_p\mathcal{B}\mathbf{M} - r\mathbf{M})\mathbf{c}_{j+1} = -k_m\mathbf{M}\mathbf{b}_j \\
&\quad + ((\tau/2)\mathbf{M} + D_c\mathbf{K} - k_p\mathcal{B}\mathbf{M} + r\mathbf{M})\mathbf{c}_j \\
&\quad - 2r\mathbf{M}c_0 + 2k_p\mathbf{N}(\mathbf{c},\mathbf{b}) - 2\mathbf{N}(\mathbf{GCa}, m_\infty^{Ca}(\mathbf{v}), \mathbf{v} - E_{Ca})/(aF)
\end{aligned} \tag{A.16}$$

where $\mathbf{b}_1 = \frac{\mathcal{B}c_0}{K_D + c_0}$ and $\mathbf{c}_1 = c_0$ are given by the rest conditions. The contribution of the voltage gated calcium channels is negligible since

$$m_\infty^{Ca}(\mathbf{v}_1) \approx 0\,. \tag{A.17}$$

A sparse LU factorization was computed to calculate the above matrix inversions. The `lu` function in `MATLAB` was used which implements the associated matrix decomposition via *UMFPACK*. In figure A.2, we show the solution to the branched equations. In this neuronal geometry, the potassium conductance increases with distance from the soma. As a result, the action potential away from the soma are significantly attenuated. The convergence properties of our scheme with respect to the space and time discretizations were studied numerically. The results are shown in figure A.3 and figure A.4. In figure A.3, we show the effect of our simplifying assumption in

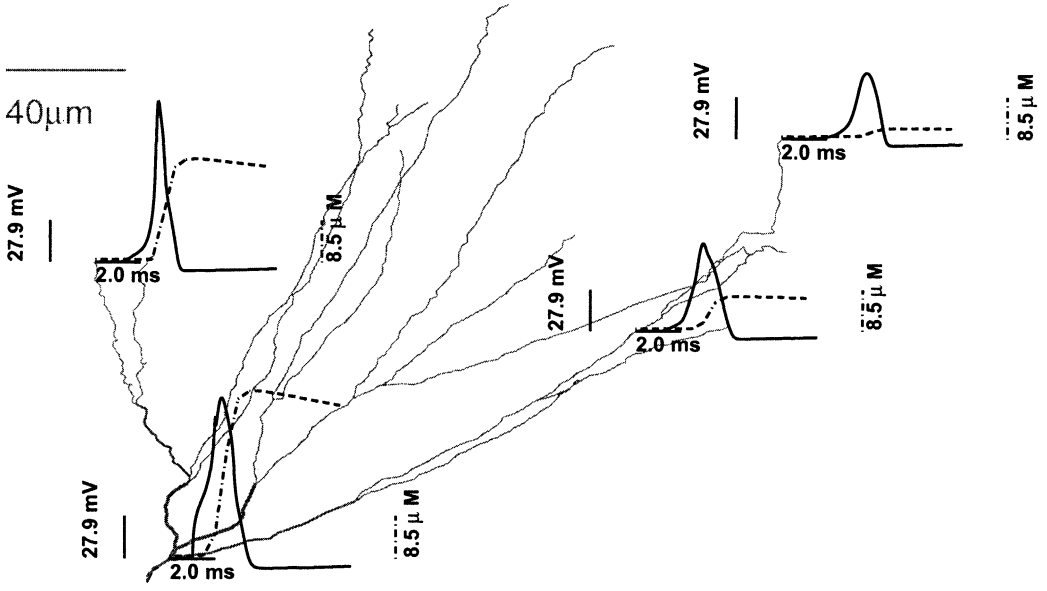

Figure A.2: The solution to the voltage-calcium system is shown with the time series at several points plotted on top of their dendritic location. The left hand axis is in mV while the right is in μM. In this particular example, potassium channel densities are quadrupling at a constant rate away from the soma. As a result, the voltages and calcium bound buffer diminish away from the soma.

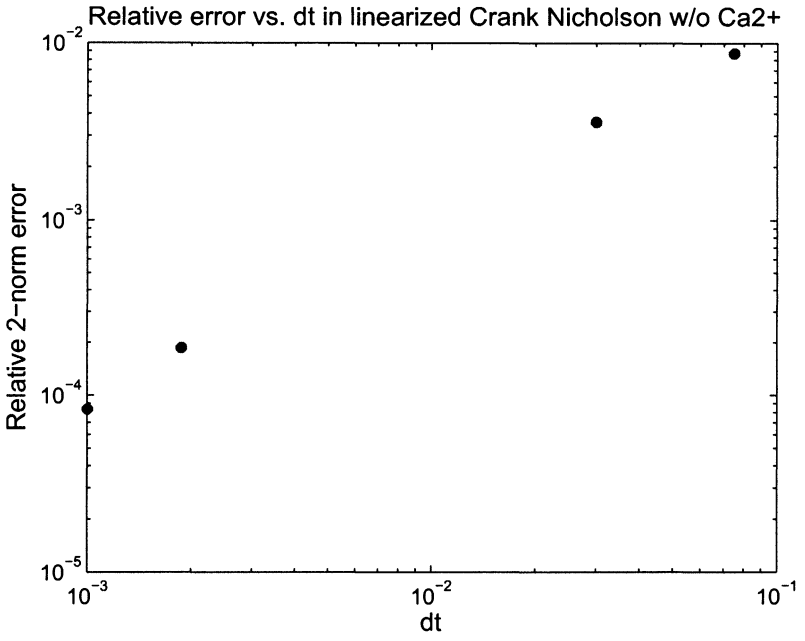

Figure A.3: The finite element method showed linear convergence with respect to dt to itself.

(A.7). The time marching scheme shows only first order convergence. In figure A.4, compares the finite element solution to a finite difference solution from Cox. Here, the spatial step size is denoted by h and the time step size by dt. Our solution shows convergence in both space and time to the finite difference solution. Additionally, we are able to recover 2 digits of accuracy in our solution using reasonable step sizes.

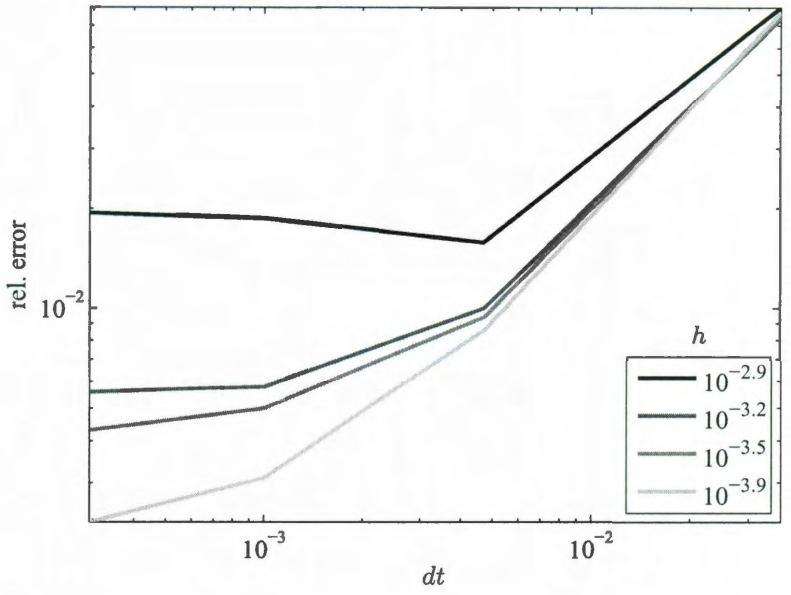

Figure A.4: Convergence results in both dt and h are shown with respect to the finite difference solution. Four different spatial discretizations were compared against the finite difference solution. The relative 2-norm error for different time discretizations are plotted.

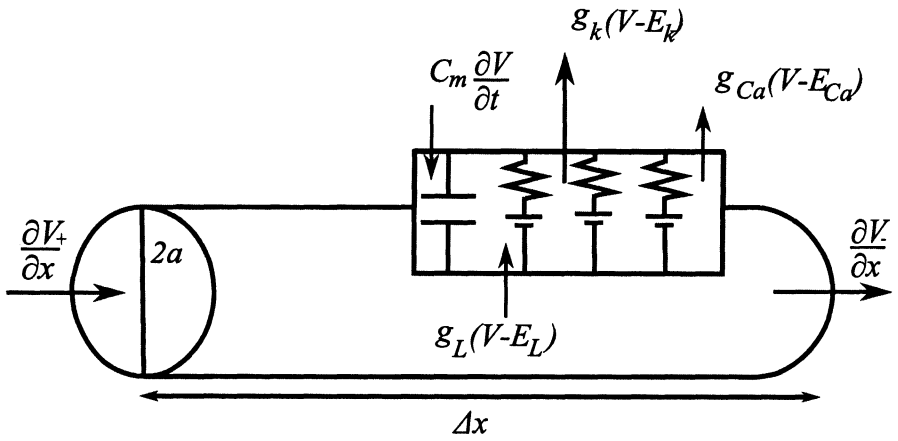

Figure A.5: A small neuronal patch of radius, a, showing all currents we wish to track. There is a flux from the left and right boundary and contributions from different channels. The outward flux by convention is denoted positively.

A.2 Derivation of the cable equation

In order to derive (2.1), we account for all the current in a patch of neuron by applying Kirchhoff's Law and using Ohm's Law. Consider the following patch of neuron in A.2. The fiber of radius a has a left flux density by J_-, the right flux density by J_+, the capacitive flux density, I_{Cm}, and channel flux density, I_{Ch}, then current balance says

$$2\pi a \Delta x C_m I_{Cm} + \frac{\pi a^2}{R}(-J_+ + J_-) + 2\pi a \Delta x I_{Ch} = 0\,. \tag{A.18}$$

We now substitute $\partial_x V = J$, and divide through by $2\pi a \Delta x$ to get

$$C_m \partial_t V + \frac{a}{2R}\frac{-\partial_x V_+ + \partial_x V_-}{\Delta x} + I_{Ch} = 0 \tag{A.19}$$

which simplifies to the cable equation when we let $\Delta x \to 0$

$$C_m \partial_t V - \frac{a}{2R}\partial_{xx} V + I_{Ch} = 0\,. \tag{A.20}$$

A.3 Derivation of the calcium system

We model calcium in the same way we derived the cable equation. Instead of using Ohm's Law to derive voltage from current, we use mass action to help keep track

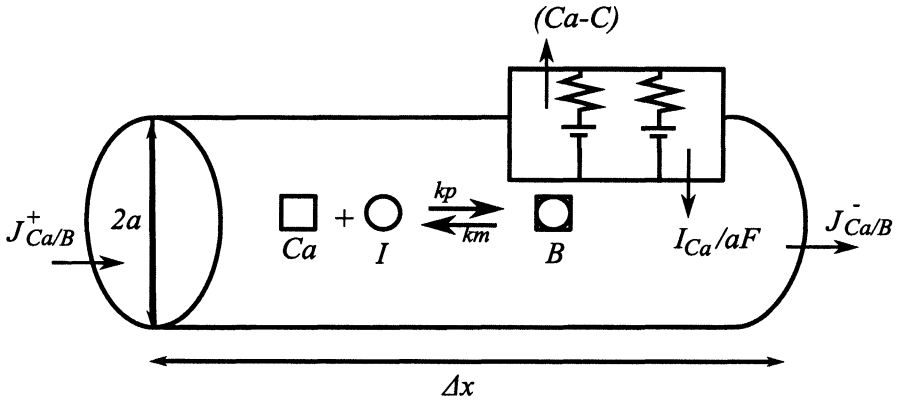

Figure A.6: A small neuronal patch showing all the sources of Ca. By convention, the outward flux is denoted positively.

of all the calcium currents in a patch of neuronal fiber. Again, we consider a patch of radius a and length, Δx, shown in A.3 with left, J_- and right, J_+. boundary calcium currents due to diffusion, calcium channels, I_{Ch}, and calcium current from the unbinding of the calcium-buffer complex, b, into calcium, c, and buffer, B where the currents are give in molar density. Since the time rate of change of calcium in the entire volume is equal to the total current, we get

$$\pi a^2 \Delta x \partial_t c = \pi a^2 D_c (J_+ - J_-) - \pi a^2 \Delta x (k_p c(\mathcal{B} - b) - k_m b) + 2\pi a \Delta x I_{Ch} \qquad \text{(A.21)}$$

where by convention we consider all inward calcium current to be negative. By dividing through by $\pi a^2 \Delta x$ and letting $\Delta x \to 0$, we get the following reaction diffusion equation

$$\partial_t c = D_c \partial_{xx} c - k_p c(\mathcal{B} - b) + k_m b + 2\frac{I_{Ch}}{a} \qquad \text{(A.22)}$$

where $\mathcal{B}$ is the total buffer concentration. We have assumed the diffusional constant of calcium, D_c, is not spatially dependent. By following a similar current balance procedure, we arrive at an analogous equations for the calcium bound buffer

$$\partial_t b = D_b \partial_{xx} b + k_p c(\mathcal{B} - b) - k_m b\,. \qquad \text{(A.23)}$$

We now parse I_{Ch} into the following currents due to voltage sensitive calcium channels and membrane bound passive pumps

$$I_{Ch} = -2\pi\frac{rc + r_0c_0}{a} - 2\pi\frac{I_{Ca}}{aF} \approx -2\pi\frac{r(c - c_0)}{a} - 2\pi\frac{I_{Ca}}{aF} \tag{A.24}$$

where F is Faraday's constant that converts coulombs into moles, I_{Ca} is the voltage dependent calcium current, r is the rate at which a passive pump brings calcium back to the steady-state calcium concentration, c_0.

A.4 Parameters and functions

Table A.1: Functional and parameters associated with the Hodgkin-Huxley [33] formulation.

Parameter	Value	Function
l	0.125 cm	$I(t) = \max(t-1,0)^3 \exp(-4\max(t-1,0))$
a	1e-4 cm	$g_L(x) = 0.3$ mS/cm^2
C_m	1 μF/cm^2	$g_K(x) = (36 + 1440x)$ mS/cm^2
R_i	0.34 kω-cm	$g_{Ca}(x) = (768x^2 - 96x + 9)$ mS/cm^2
E_L	-54.387 mV	$g_{Na}(x) = 120$ mS/cm^2
E_K	-77 mV	$w_\infty(v) = 1 + \tanh((v+1)/15)/2$
E_{Ca}	100 mV	$n_\alpha(v) = 0.01(v+55)/(1 - \exp(-0.1(v+55)))$
E_{Na}	50 mV	$n_\beta(v) = 0.125\exp(-0.0125(v+65))$
		$h_\alpha(v) = 0.07\exp(-0.05(v+65))$
		$h_\beta(v) = 1/(1 + \exp(-0.1(v+35)))$
		$m_\alpha(v) = 0.1(v+40)/(1 - \exp(-0.1(v+40)))$
		$m_\beta(v) = 4\exp(-0.0556(v+65))$

Bibliography

[1] N.F. al Baldawi and R.F. Abercrombie. Cytoplasmic calcium buffer capacity determined with nitr-5 and dm-nitrophen. *Cell Calcium*, 17:409–421, 1995.

[2] E. Ballou, Bryan Smith, R. Anelli, and C. Heckman. Measuring dendritic distribution of membrane proteins. *J. Neurosci. Meth.*, 156:257–266, 2006.

[3] J. Bell and G. Craciun. A distributed parameter identification problem in neuronal cable theory. *Mathematical Biosciences*, 194(1):1–19, March 2005.

[4] George H. Bishop. Natural history of the nerve impulse. *Physiol. Rev.*, 36:376–399, 1956.

[5] Alexander Borst and Henery Abarbanel. Relating a calcium indicator signal to the unperturbed calcium concentration time-course. *Theor. Bio. Med. Mod.*, 4:1–13, 2007.

[6] Marco Canepari and Fabio Mammano. Imaging neuronal calcium fluorescence at high spatio-temporal resolution. *J. Neurosci. Meth.*, 87:1–11, 1999.

[7] R. G. Carter. On the global convergence of trust region algorithms using inexact gradient information. *SIAM J. Numer. Anal.*, 28:251–265, 1991.

[8] C.M. Colbert, J.C. Magee, D.A. Hoffman, and D. Johnston. Slow recovery from inactivation of na+ channels underlies the activity-dependent attenuation of den-

dritic action potentials in hippocampal ca1 pyramidal neurons. *J. Neurosci.*, 17:6512–6521, 1997.

[9] Kenneth S. Cole. *Membranes, ions, and impulses.* Biophysics series;, v.1. University of California Press, 1968.

[10] Thomas Coleman and Yuying Li. An interior trust region approach for nonlinear minimization subject to bounds. *SIAM J. Optim.*, 6:418–445, 1996.

[11] Steven J. Cox. A new method for extracting cable parameters from input impedance data. *Mathematical Biosciences*, 153(1):1–12, October 1998.

[12] Steven J. Cox. Estimating the location and time course of synaptic input from multi-site potential recordings. *Journal of Computational Neuroscience*, 17(2):225–243, September 2004.

[13] Steven J. Cox. An adjoint method for channel localization. *Math Med Biol*, 23(2):139–152, 2006.

[14] Steven J. Cox. Direct correction of non-spaced-clamped currents via cole's theorem. *J. Neurosci. Meth.*, 169:368–373, 2007.

[15] Steven J. Cox and Boyce E. Griffith. Recovering quasi-active properties of dendritic neurons from dual potential recordings. *Journal of Computational Neuroscience*, 11(2):95–110, September 2001.

[16] Steven J. Cox and Lin Ji. Identification of the cable parameters in the somatic shunt model. *Biological Cybernetics*, 83(2):151–159, July 2000.

[17] Steven J. Cox and Jay H. Raol. Recovering the passive properties of tapered dendrites from single and dual potential recordings. *Mathematical Biosciences*, 190(1):9–37, July 2004.

[18] Peter Craven and Grace Wahba. Smoothing noisy data with spline function. *Numer. Math.*, 31:377–403, 1979.

[19] Ivar Ekeland and Roger Teman. *Convex analysis and variational problems.* SIAM, 1999.

[20] G.C. Ellis-Davies, Kaplan J.H., and R.J. Barsotti. Laser photolysis of caged calcium: rates of calcium release by nitrophenyl-egta and dm-nitrophen. *Biophys. J.*, 70:1006–1016, 1996.

[21] David D. Friel and Hillel J. Chiel. Calcium dynamics: analyzing the ca2+ regulatory network in intact cells. *Trends Neurosci.*, 31:8–19, 2008.

[22] M. Gabso, E. Neher, and M. Spira. Low mobility of the ca2+ buffers in axons of cultured aplysia neurons. *Neuron*, 18:472–481, 1997.

[23] Allan T. Gulledge, Bjorn M. Kampa, and Greg J. Stuart. Synaptic integration in dendritic trees. *J. Neurobio.*, 64:75–90, 2005.

[24] E. Haber, Uri Ascher, and D. Oldenburg. On optimization techniques for solving nonlinear inverse problems. *Inverse Problems*, 16:1263–1280, 2000.

[25] Martin Hanke and Otmar Scherzer. Inverse problems light: numerical differentiation. *The American Mathematical Monthly*, 108:512–521, 2001.

[26] Yuan He and David Keyes. Reconstructing parameter of the fitzhugh-nagumo system from boundary potential measurements. *J. Comput. NeuroSci*, 23:251–264, 2007.

[27] Yuan He and David Keyes. Pde-based parameter reconstruction through schur and schwarz decomposition. *Lect. Not. Comp. Sci. Engi.*, 60:543–550, 2008.

[28] Donald Hebb. *The organization of behavior.* Lawrence Erlbaum Associates, 1949.

[29] C. Heinemann, R.H. Chow, E. Neher, and R.S. Zuker. Kinetics of the secretory response in bovine chromaffin cells following flash photolysis of caged ca2+. *Biophys. J.*, 67:2246–2557, 1994.

[30] F. Helmchen, K. Imoto, and B. Sakmann. Ca2+ buffering and action potential-evoked ca2+ signaling in dendrites of pyramidal neurons. *Biophys. J.*, 70:1069–1081, 1996.

[31] M. Hines. Efficient computation of branched nerve equations. *Int. J. Bio-Medical Computing*, 15:69–76, 1984.

[32] M.L. Hines and N.T. Carnevale. The neuron simulation environment. *Neural Computation*, 9(6):1179–1209, August 1997.

[33] A. L. Hodgkin and A. F. Huxley. A quantitative description of membrane current and its application to conduction and excitation in nerve. *The Journal of Physiology*, 117(4):500–544, 1952.

[34] Vijay Iyer, Tycho M. Hoogland, and Peter Saggau. Fast functional imaging of single neurons using random-access multiphoton (ramp) microscopy. *J Neurophysiol*, 95(1):535–545, 2006.

[35] Daniel Johnston and Rishikesh Narayanan. Active dendrities: colorful wings of the mysterious butterflies. *Trends Neurosci.*, 31:309–316, 2008.

[36] Bjorn M. Kampa, Johannes J. Letzkus, and Greg J. Stuart. Dendritic mechanisms controlling spike-timing-dependent synaptic plasticity. *Trends Neurosci.*, 30:456–463, 2007.

[37] J. Keener and J. Sneyd. *Mathematical physiology.* Springer, 2001.

[38] Wagner J. Keizer. Effects of rapid buffers on ca2+ diffusion and ca2+ oscillations. *Biophys. J.*, 67:447–456, 1994.

[39] A. Kellems, D. Roos, N. Xiao, and S. J. Cox. Low-dimensional, morphologically accurate models of subthreshold membrane potential. *J. Comput. Neurosci.*, 2009.

[40] Christof Koch. *Biophysics of computation: information processing in single neurons.* Oxford University Press, 1999.

[41] Christof Koch and Idan Segev. *Methods in neuronal modeling: from ions to networks.* MIT Press, 1998.

[42] P.G. Kostyuk and A.N. Verkhratsky. *Calcium signaling in the nervous system.* John Wiley & Sons, 1995.

[43] H. Larsson, S. Kleene, and H. Lecar. Noise analysis of ion channels in non-spaced-clamped cables: estimates of channel parameters in olfactory cilia. *Biophys. J.*, 1997:1193–1203, 1997.

[44] J.L. Lions. *Optimal control of systems governed by partial differential equations.* Springer-Verlag, Berlin, 1971.

[45] Michael London and Michael Husser. Dendritic computation. *Annu. Rev. Neurosci.*, 28(1):503–, July 2005.

[46] Michael Mascagni. The backward euler method for numerical solutions of the hodgkin-huxley equations of nerve conduction. *SIAM J. Numer. Anal.*, 27(4):941–962, August 1990.

[47] Warren S. McCulloch and Walter Pitts. A logical calculus of the ideas immanent in nervous activity. *Bull. Math. Biol.*, 5:115–133, 1943.

[48] Lidia A. Mironova and L. Mironov, Sergej. Approximate analytical time-dependent solutions to describe large-amplitude local calcium transients in the presence of buffers. *Biophys. J.*, 94:349–358, 2008.

[49] M. Naraghi. Kinetics of the secretory response in bovine chromaffin cells following flash photolysis of caged ca2+. *Cell Calcium*, 22:255–268, 1997.

[50] M. Naraghi, T.H. Muller, and E. Neher. Two-dimensional determination of the cellular ca2+ binding in bovine chromaffin cells. *Biophys. J.*, 75:1635–1647, 1998.

[51] E. Neher. The use of fura-2 for estimating ca buffers and ca fluxes. *Neuropharm.*, 34:255–268, 1995.

[52] E. Neher and G. J. Augustine. Calcium gradients and buffers in bovine chromaffin cells. *J. Physiol.*, 450:273–301, 1992.

[53] Erwin Neher. Calcium buffers in flash-light. *Biophys. J.*, 79:2783–2784, 2000.

[54] Jorge Nocedal and Stephen Wright. *Numerical Optimization.* Springer, 2006.

[55] M. Patterson, J. Sneyd, and D. Friel. Depolarization-induced calcium release response in sympathetic neurons: relative contributions from ca2+ entry, extrusion, er/mitochondrial ca2+ uptake and release, and ca2+ buffering. *J. Gen. Physiol.*, 129:29–56, 2006.

[56] D.J. Perkel, J. J. Petrozzino, R.A. Nicoll, and Connor J. A. The role of ca2+ entry via synaptically activated nmda receptors in the induction of long-term potentiation. *Neuron*, 11:817–823, 1993.

[57] A. Pippow, A. Husch, C. Pouzat, and P. Kloppenburg. Differences of ca2+ handling properties in identified central olfactory neurons of the antennal lobe. *Cell Calcium*, 46:87–98, 2009.

[58] S. Ramaswamy, F. Baroni, P. Varnoa, and G. de Polavieja. Time-scales in the interplay between calcium and voltage dynamics. *Neurocomputing*, 70:10–12, 2007.

[59] A. Schaefer, M. Helmstaedter, B. Sakmann, and A. Korngreen. Correction of conductance measurements in non-spaced-clamped structures: 1. voltage-gated k+ channels. *Biophys. J.*, 84:3508–3528, 2003.

[60] A. Schaefer, M. Helmstaedter, A. Schmitt, B. Bar-Yehuda, M. Almog, H. Ben-Porat, B. Sakmann, and A. Korngreen. Dendritic voltage-gated k+ conductance gradient in pyramidal neurons of neocortical layer 5b from rats. *J. Physiol.*, 579:737–752, 2006.

[61] Idan Segev, John Rinzel, and Gordon M. Shepherd, editors. *The theoretical foundation of dendritic function: selected papers of Wilfrid Rall with commentaries.* MIT Press, 1994.

[62] Nelson Spruston. Pyramidal neurons: dendritic structure and synaptic integration. *Nat. Rev. Neurosci.*, 9:206–211, 2008.

[63] N. Stockbridge. Solution of the hodgkin-huxley and cable equations on an array processor. *Annals of Biomedical Engineering*, 17(3):253–268, May 1989.

[64] Greg Stuart, Nelson Spruston, and Michael Hausser, editors. *Dendrites.* Oxford University Press, 2007.

[65] J. Wagner and J. Keizer. Effects of rapid buffers on ca2+ diffusion and ca2+ oscillations. *Biophys. J.*, 67:447–456, 1994.

[66] J. Waters, A. Schaefer, and B. Sakmann. Backpropagating action potentials in neurones: measurement, mechanisms and potential functions. *Prog. Biophys. Mol. Bio.*, 87:145–170, 2004.

[67] Jack Waters. Caught on film: the secret lives of dendrites in the tadpole optic tectum. *Neuron*, In Press, 2009.

[68] R. Westenbroek. Ion channel localization in cell bodies and dendrites. In Larry R. Squire, editor, *Encylopedia of neuroscience*, pages 221–228. Academic Press, 2008.

[69] T. Xu, M. Naraghi, H. Kang, and E. Neher. Kinetic studies of ca2+ binding and ca2+ clearance in the cytosol of adrenal chromaffin cells. *Biophys. J.*, 73:532–545, 1997.

[70] Lily M. Yu and Yukiko Goda. Dendritic signaling and homeostatic adaptation. *Curr. Opin. Neurobio.*, In Press, 2009.

[71] Z. Zhou and E. Neher. Mobile and immobile calcium buffers in bovine adrenal chromaffin cells. *J Physiol.*, 469:245–273, 1993.